


NANO EXPRESS

Open Access



Au@Ag Core@Shell Nanoparticles Synthesized with *Rumex hymenosepalus* as Antimicrobial Agent

Jesús Mauro Adolfo Villalobos-Noriega¹, Ericka Rodríguez-León^{1*}, César Rodríguez-Beas¹, Eduardo Larios-Rodríguez², Maribel Plascencia-Jatomea³, Aarón Martínez-Higuera¹, Heriberto Acuña-Campa⁴, Alfonso García-Galaz⁵, Roberto Mora-Monroy⁶, Francisco Javier Alvarez-Cirerol⁷, Blanca Esthela Rodríguez-Vázquez⁸, Roberto Carlos Carillo-Torres¹ and Ramón A. Iñiguez-Palomares^{1*} 

Abstract

In this work, we used a sequential method of synthesis for gold–silver bimetallic nanoparticles with core@shell structure (Au@AgNPs). *Rumex hymenosepalus* root extract (Rh), which presents high content in catechins and stilbenes, was used as reductor agent in nanoparticles synthesis. Size distribution obtained by Transmission Electron Microscopy (TEM) gives a mean diameter of 36 ± 11 nm for Au@AgNPs, 24 ± 4 nm for gold nanoparticles (AuNPs), and 13 ± 3 nm for silver nanoparticles (AgNPs). The geometrical shapes of NPs were principally quasi-spherical. The thickness of the silver shell over AuNPs is around 6 nm and covered by active biomolecules onto the surface. Nanoparticles characterization included high angle annular dark field images (HAADF) recorded with a scanning transmission electron microscope (STEM), Energy-Dispersive X-ray Spectroscopy (EDS), X-Ray Diffraction (XRD), UV–Vis Spectroscopy, Zeta Potential, and Dynamic Light Scattering (DLS). Fourier Transform Infrared Spectrometer (FTIR), and X-ray Photoelectron Spectroscopy (XPS) show that nanoparticles are stabilized by extract molecules. A growth kinetics study was performed using the Gompertz model for microorganisms exposed to nanomaterials. The results indicate that AgNPs and Au@AgNPs affect the lag phase and growth rate of *Escherichia coli* and *Candida albicans* in a dose-dependent manner, with a better response for Au@AgNPs

Keywords: Au@Ag core@shell nanoparticles, *Rumex hymenosepalus*, Gompertz model, Lag phase

Introduction

In the last 25 years, several chemical methods have been studied for nanomaterial synthesis; however, most of these methods use substances that are unfriendly to the environment and use high temperatures or expensive equipment. In this work, we performed the synthesis of gold–silver nanostructures by using the green synthesis method. This method minimizes pollution from the

beginning. Using "clean" processes, avoiding most of the waste and use of hazardous pollutants in developing "clean" nanomaterials that do not pose a threat to health or the environment.

Green synthesis of metal nanoparticles seeks a positive influence of the interaction with biological systems, which means that nanoparticles and their self-functionalization with polyphenol molecules generate biological interactions compatible with systems such as cells and macromolecules. In general, these biological interactions are used as nanomedicine for diseases such as cancer, diabetes, and neurodegenerative diseases. The synthesis of silver (shell) and AuNPs as a core–shell system has applications such as optical diagnostic sensors, molecular

*Correspondence: ericka.rodriguez@unison.mx; ramonalfonso.iniguez@gmail.com

¹ Nanotechnology Graduate Program, Department of Physics, University of Sonora, Rosales and Transversal, 83000 Hermosillo, Sonora, Mexico
Full list of author information is available at the end of the article

sensor [1, 2], photothermal therapies, antimicrobials and improves the catalytic process [3–6] compared with monometallic NPs.

In particular, sequential or simultaneous methods in different reactors, chemical and physical methods [7] are used for the bimetallic synthesis: ultrasonic spray pyrolysis[8], a sonochemical method[5], a microfluidic chip [9], sequential nanofluidic nanoprecipitation [10, 11] micro-emulsions[12], liposomes [13], reducing agents used are chemical or green chemical types.

Dry materials are used in nanoparticles synthesis as metal oxides [14], carbon nanotubes [15, 16], other uses printed soft electronic devices [17]. Wet, nanoparticles used on biological systems [18–20] drugs carrier [21, 22], antimicrobial [23, 24], sensing application [25] and Computational nanotechnology are a modern classification [26] used to define uses.

Khatami et al., reviewed the green synthesis using plants of core@shell-type nanoparticles, in particular, were used *Antigonon leptopus*, *Diopyros kaki*, *Azadirachta indica*, *Potamogeton pectinatus*, *Anacardium occidentale* for the synthesis of Au@Ag nanoparticles with size between 5 and 500 nm (a), were tested for different applications (non-antibacterial), and *Asparagus racemosus* Root Extract was used to synthesis of Au–Ag alloy nanoparticles finding a MIC at 480 µg/mL tested in *Escherichia coli*, *Bacillus subtilis*, *Klebsiella pneumonia*, *Pseudomonas aeruginosa*, and *Staphylococcus aureus* [27]. Au@Ag NPs obtained by chemical synthesis have applications as antibacterial, and the MIC reported is around 2.5 µg/mL for silver content (shell) [28], Lu et. al. reported a chemical synthesis of Au/AgNPs@Van were prepared using NaBH₄ and addition Vancomycin and MIC was 60 nmol/mL for nanoparticles bimetallic tested in gram-positive and negative bacteria [29].

Antibacterial properties of bimetallic nanomaterials [30–34] improve as a function of the concentration of Ag. In contrast, an increment in Au concentration decreases the antibacterial properties but reduces the cytotoxic effect, i.e., the bimetallic material becomes more biocompatible [35]. Comparing the effect of Au and Ag monometallic materials with bimetallic materials [36–40], it has been demonstrated that a synergistic effect [41] occurs between bimetallic materials, generating bifunctional effects [28, 42].

Nanomaterials functionalization has particular interest since the chemical environment [43–45] (pH, presence of sulfur, biocompatible molecules, etc.) surrounding the system will have effects on the interaction with cells or microorganisms; therefore, the emphasis on generating biomaterials using green chemistry [46–55].

The chemical composition of the bimetallic particles [56–58] will be a determining factor in their

optical properties [41, 59], owing to the synergistic effect of monometallic nanostructures [60].

In this work, gold and silver nanoparticles were synthesized using as a reductor agent a *Rumex hymenosepalus* extract, which is a plant that contains stilbenes and catechins molecules that act as powerful antioxidants in reducing metal ions. Gold nanoparticles were used as nuclei to obtain bimetallic nanoparticles core@shell type of Au@Ag through a sequential synthesis method. The characterization of nanomaterials involves the techniques of HAADF-STEM, TEM with EDS y HRTEM.

With the different types of synthesized nanoparticles, a comparative study was carried out on the growth dynamics of the bacteria *E. coli* and *S. aureus* and the yeast *Candida albicans*.

Experimental Section

Materials

The roots of *Rumex hymenosepalus* were acquired in a commercial establishment of the locality. Both precursors HAuCl₄ and AgNO₃ for nanoparticle synthesis were purchased from Sigma-Aldrich with a purity of 99%. Brain Heart Infusion (BHI) Broth and Potato Dextrose Broth (PDB) used for microorganism assays were procured from Sigma-Aldrich. Ethanol (99% pure) used in the cleaning nanoparticles process was acquired from Fermont, and ultrapure water (milli-Q) was used in experiments.

Rumex hymenosepalus Extract

For extract preparation, 150 g of root cut into slices and previously dehydrated were macerated in 1000 mL of a 70/30 V/V ethanol/water mixture. The maceration was carried out at room temperature in a glass container with a hermetic stopper and protected from light. The absorbance of the solution obtained was monitored for 21 days until there were no changes in its value. At this time, the maceration process was considered finished. The extract obtained was successively filtered with Whatman paper filters with pore sizes of 8 µm and 2 µm and finally with an acrodisc filter of 0.22 µm. Ethanol was removed by rotovaporation, and the aqueous extract concentrate was frozen at -80 °C for lyophilization (Labconco, FreeZone 1L). The powders obtained were stored in sterile containers protected from light at room temperature until use.

Synthesis of AuNPs

Firstly, *Rumex hymenosepalus* aqueous solution was prepared at 10 mg/mL from the lyophilized extract. Later 16 mL of *Rumex* solution was mixed with 32 mL of ultrapure water, keeping agitation at 1000 rpm and were added slowly 16 mL of HAuCl₄ (0.01 M). The reaction was held for one hour under laboratory lighting

conditions and at room temperature. The intensity of surface plasmon resonance ($\lambda_{\text{SPR}} = 540$ nm) was evaluated by UV–Vis spectroscopy over time; when no change was observed, the synthesis was considered complete. The obtained product was centrifuged at 12,000 rpm, the supernatant was replaced by ultrapure water, and a sonication process was applied for 1 h to redisperse nanoparticles. The procedure was repeated three times more. Water was used as a solvent on the first two occasions and ethanol on the last. Finally, ethanolic dispersion was centrifuged, and precipitates dried in a convection oven at 40 °C to prepare an AuNPs aqueous dispersion at 2300 µg/mL.

Synthesis of Au@AgNPs

For Au@AgNPs synthesis, 2 mL of the AuNPs aqueous dispersion (2300 µg/mL), 0.8 mL of AgNO₃ (0.1 M), and 0.8 mL of *Rumex hymenosepalus* solution (10 mg/mL) were deposited in a sterile glass culture tube. The mixture was sonicated for 3 h in an ultrasonic cleaner bath (Branson, Model 2510). Later, the content was centrifuged at 12,000 rpm for one hour, solids obtained were redispersed in ultrapure water by sonication to obtain a 1000 µg/mL concentration.

Synthesis of AgNPs

To produce AgNPs, 16 mL of extract solution (10 mg/mL) was mixed with 64 mL of ultrapure water, and 8 mL of AgNO₃ 0.1 M. The reaction was carried out for one hour under laboratory lighting conditions at 25 °C, and surface plasmon resonance ($\lambda_{\text{SPR}}^{\text{Ag}} = 440$ nm) was monitored by UV–Vis spectroscopy over time to assess formation. The product was centrifuged at 12,000 rpm, the supernatant was replaced by ultrapure water, and sonication was applied for 1 h. The procedure was repeated three times more. Water was used as a solvent on the first two occasions and ethanol on the last. Ethanolic dispersion was centrifuged and precipitates dried in a convection oven at 40 °C. Finally, AgNPs dust obtained was redispersed in ultrapure water by sonication to generate a colloidal dispersion at 2000 µg/mL concentration.

Characterizations

UV–Vis absorption spectra were obtained on a dual-beam PerkinElmer Lambda 45 spectrometer. A slit of 0.5 nm was employed, and spectra were recorded at a speed of 480 nm/min in a range between 200 and 900 nm. For the nanoparticles, 50 µL of sample and only 5 µL for the extract were used. The final volume was made up to 3 mL in the quartz cells using ultra-pure water as solvent.

Zeta potential (ζ) of AuNPs, AgNPs, and Au@AgNPs were measured using a Zetasizer-Nano ZS (Malvern Instruments, UK). Each sample was measured at room

temperature (25 °C) in triplicate and as a function of concentration at 1, 10, 50, and 100 µg/mL for each sample.

DLS for AuNPs, AgNPs, and Au@AgNPs were measured using a Zetasizer-Nano ZS (Malvern Instruments, UK) equipped with a 633 nm He–Ne laser. Each sample was measured at room temperature (25 °C) in triplicate and as a function of concentration at 1, 10, 50, and 100 µg/mL for each sample. Polydispersity Index (PDI) was determined from DLS experiments using Malvern software through the definition $\text{PDI} = \left(\frac{\sigma}{D}\right)^2$, where D is the average Diameter and σ is the standard deviation of D . PDI values with 0.10 or less are considered highly monodisperse [62].

The optical band gap E_g was calculated for AgNPs, AuNPs, Ag@AuNPs, using Tauc equation determine a bandgap in materials by the following relationship:

$$\alpha = \frac{c}{h\nu} (h\nu - E_g)^{1/n} \quad (1)$$

where α is the absorption coefficient of the material ($\alpha = 2.303 A/d$ where A is absorbance and d is the width of the cell) and where E_g is the optical energy band gap and $h\nu$ is the photon energy obtained by drawing a line between $(\alpha h\nu)^n$ and photon energy $h\nu$. The index number n is taken as 2 for the allowed direct band to band transitions in samples [63] and can be readily evaluated with a linear fit plot [64]. Depends upon the type of the transition which may have values 1/2, 2, 3/2, and 3 correspond to the allowed direct, allowed indirect, forbidden direct, and forbidden indirect transitions, respectively [65].

Samples AgNPs, AuNPs, Ag@AuNPs, and Rh were analyzed through infrared absorption using an FTIR (PerkinElmer, Inc., Waltham, Spectrum Two). The acquisition parameters were: 4 cm^{−1} resolution, 16 scans, and between 4000 and 900 cm^{−1} wavelength range.

X-ray photoelectron spectroscopy assays were carried out on a PerkinElmer model PHI 5100, which contains a dual source of Mg/Al, 300 W, 15 kV. The Mg K α emission line with the energy of 1253.6 eV was used for AgNPs, AuNPs, Ag@AuNPs, and Rh. All experiments were performed under vacuum conditions of 2×10^{-9} Torr. [66]. Data were analyzed using Multipak software. For XPS characterization, the different nanoparticle dispersions and the *Rumex hymenosepalus* extract solution were deposited on clean coverslips as follows. 30 µL of the sample was added to the coverslip allowing it to dry completely for the next deposit. The process was repeated at least 5 times until a thin film was formed and then characterized by XPS.

High-Angle Annular Dark Field-Scanning Transmission Electron Microscopy (HAADF-STEM) can be considered a powerful operation mode in electron

microscopy, which provides a large amount of complementary information elucidates the structure of a nanomaterial. Aberration-corrected HAADF-STEM can determine with atomic resolution the positions of atoms of different chemical nature. This is due to aberration-corrected HAADF-STEM, known for its chemical sensitivity and high spatial resolution [67]. In this operation mode, the incoherent image is dominant with a negligible contribution of diffraction contrast [68]. Thus, atomic number contrast (Z contrast) in HAADF-STEM aberration-corrected allows us to determine the structural details of nanostructures with great precision.

For STEM analysis, samples were analyzed in a JEOL-JEMARM200 electron microscope operating at 200 kV, with a CEOS-corrector for the condenser lens. Z-Contrast STEM images were recorded simultaneously in both BF and HAADF modes. Images were recorded with a 40-micron condenser lens aperture (32–36 mrad convergence angle) and a spot size of 9 pA.

For electron microscopy analysis, a drop (10 μ L) of Au@AgNPs suspension was deposited on a 300-mesh thick carbon grid, dried to room temperature, and placed in a vacuum chamber for 24 h.

Nanoparticles were analyzed by TEM in Jeol 2010F apparatus (1.9 Å resolution) at 200 kV. EDS analysis was realized using a QUANTAX 200-TEM X-ray spectrometer (Bruker) with XFlash 4010 detector. For HRTEM analysis, TEM micrographs were recorded at magnifications greater than 100,000X. Interplanar spacings of crystal planes were determined by digital micrograph analysis (3.0 Gatan Version). Sample preparation was similar to that described above for STEM analysis.

Data were collected using a Bruker D8 QUEST diffractometer system equipped with a Multilayer mirrors monochromator and a Cu K α Microfocus sealed tube ($\lambda = 1.54178$ Å). Frames were collected at $T = 300$ K via ω/ϕ -scans and then processed to obtain diffractograms of Intensity vs. 2Theta. High Score Plus software was used for raw data treatment and the ICSD powder diffraction database associated with software was implemented for the search-match phase identification analyses.

Antibacterial Activity Assay

Microorganisms tested were bacteria *Escherichia coli* (ATCC 25922), *Staphylococcus aureus* (ATCC 5538P), and yeast *Candida albicans* isolated from infected urine collected from an adult male patient with urinary tract infection (our study follow the principles of the Declaration of Helsinki). Brain Heart Infusion (BHI) and Potato Dextrose Broth (PDB) were used to prepare inoculum of bacteria and yeast, respectively. Cultures were incubated at 37 °C overnight. The concentration in colony-forming units (CFU/mL) per milliliter of

suspension was determined by measuring the optical density by UV–Vis at 540 nm for bacteria, 600 nm for yeast. Suspensions containing 4×10^8 , 7.8×10^8 , and 2.5×10^6 CFU/mL were used for *E. coli*, *S. aureus*, and *C. albicans*, respectively. Antimicrobial activity was tested in 96-well plates, using liquid culture medium added with nanoparticles and microorganism at 37 °C. All tests were performed by triplicate. Absorbance was measured in a multimode plate reader Synergy HTX Biotek, using Gen 5 software. All the microbial growth curves were performed using the Origin Lab 8.0 software. As a first step, 70 μ L of fresh broth medium (BHI or PDB, according to the studied microorganisms) mixed with nanoparticles at the required concentration were added to the wells. Later, 30 μ L of microorganism suspension was added to the wells and homogenized with the medium. The final volume on each well was 100 μ L. After dispensing the inoculum, the 96-well plates were read in the spectrophotometer described above. Plates were kept at 37 °C for 24 h, with a circular shaking mode before each reading with a period of 15 min each. The growth rate of microorganisms was determined by optical density measurement (OD) at the mentioned wavelength.

Curves Growth Analyzed by the Gompertz Model

It is well known in the literature that the Gompertz growth model well describes the growth of microorganism populations. This model allows us to understand two critical parameters in the description of the growth of the microorganism population: the adaptive phase (Lag phase) and the population growth rate. In particular, studying the behavior of the Lag phase in inhibitory treatments of microorganisms is relevant because it provides information on the adaptive responses of the microorganism to the treatment and can even give indications about the development of resistance of the microorganism to the evaluated treatment [69].

The modified Gompertz model has been described by Zwietering et al. [70] and adapted by Li et al. [69] and other authors [71–78] as a model that adjust the growth curves and

$$y = A \exp \left\{ - \exp \left[\frac{\mu e}{A} (\lambda - t) + 1 \right] \right\} \quad (2)$$

where A is the cell number expressed as OD₅₄₀ (*S. aureus* and *E. coli*) and OD₆₀₀ (*C. albicans*), μ is the growth rate at the exponential phase and e is the exponential e^1 , λ is the lag phase. We have adjusted our growth kinetic using a software origin 9.1 to analyze the effects over *S. aureus*, *E. coli*, and *C. albicans* of the three agents AuNPs, AgNPs, and Au@AgNPs.

Effect of Nanoparticles over *E. coli*, *S. aureus*, and *C. albicans* Growth

Escherichia coli and *Staphylococcus aureus* were inoculated in BHI medium, and *C. albicans* was inoculated in PD broth. All cultures were incubated overnight at 36° C. After incubation, the three cultures were adjusted to absorbance of 1, 0.7, and 1, respectively ($\lambda = 540$ nm). AuNPs, AgNPs, and Au@AgNPs were adjusted to a concentration of 50 $\mu\text{g/mL}$. In a 96 microwell plate, adjusted cultures were exposed to nanoparticles in a relationship 7:3, reaching a final volume of 200 μL each microwell. Also, adjusted cultures were exposed to sterilized water as a control condition in the same previously described conditions. Others used controls for this experiment were fresh media and each nanoparticle solutions without microorganisms. *Escherichia coli*, *Staphylococcus aureus*, and *Candida albicans* were exposed to AuNPs, AgNPs, and Au@AgNPs, respectively. Microwell plate was incubated at 36° C, and a sample of each microorganism in treatment and control conditions was obtained at 1, 7, 13, and 19 h. Collected samples were diluted in serial 1:10 saline solution and spread over Müller–Hinton plates surface. Inoculated plates were incubated at 36 °C for 24 h. After incubation, CFU/mL were calculated using direct counting.

Minimal Bactericidal Concentration (MBC) Determination

Staphylococcus aureus, *Escherichia coli*, and *Candida albicans* were inoculated each one into Müller–Hinton broth incubated overnight at 36° C and adjusted to 0.5 McFarland Nephelometer. Once inoculums were adjusted for Minimum inhibitory concentration (MIC) determination, a microdilution test was performed. Briefly, a 96-well plate was used for this purpose. 160 μL of an adjusted culture of each microorganism was poured into 5 wells. Solutions of AuNPs, AgNPs, and Au@AgNPs of 1000 $\mu\text{g/mL}$ were prepared. Previous solutions were used for preparing 750, 500, and 250 $\mu\text{g/mL}$ solutions. Pure sterilized water was used as a 0 $\mu\text{g/mL}$ of nanoparticles, and 40 μL of each previous solution was added to 160 μL of adjusted cultures. In this way, each culture was exposed to a final concentration of 200, 150, 100, 50, and 0 $\mu\text{g/mL}$ of each tested nanoparticle. The microplate was incubated at 36° C for 24 h. After that, a sample of each well was inoculated on a surface of Müller–Hinton and incubated in the same previously described conditions. After incubation, Müller–Hinton plates were observed searching for any growth signal. The concentration where no growth signals were observed was recorded as MBC value.

Results and Discussions

Characterization

Figure 1a shows the UV–vis absorption spectra of the synthesized nanomaterials. The absorbances have been normalized for the maximum localized surface plasmon resonance (LSPR) corresponding to each nanoparticle system.

Au@AgNPs absorption spectrum in Fig. 1a has a single band centered at 474 nm, which is located between the AgNPs LSPR (445 nm) and the AuNPs LSPR (544 nm). The absence of a gold-like absorption peak on Au@AgNPs suggests that obtained nanomaterials by sequential synthesis are core@shell structures. It is not possible to detect any absorption band associated with Au belongs to the nucleus. Some authors assume that for core@shell systems, the absorption spectra are composed of two bands associated with each of the metals for shell thicknesses between 3 and 4 nm. The absorption associated with metalcore disappears for higher thicknesses, obtaining a single absorption band where the maximum location depends on the thickness/core size ratio of the bimetallic particle [79, 80].

Samal et al. [81] synthesized core@shell nanoparticles (Au@Ag) by controlling the nuclei sizes and adding different thicknesses shells. In particular, our UV–vis result for Au@AgNPs coincides with that reported by Samal et al. for 32 nm gold cores and a silver thickness greater than 15 nm, where spectra are characterized by a single absorption band (~ 450 nm), and the suppression of Au surface plasmons is observed.

Additionally, in Fig. 1a, absorption centered at 280 nm (region highlighted in blue) can be observed, corresponding to molecules from the *Rumex hymenosepalus* extract used as a reducing agent in our nanoparticle synthesis. Additional file 1: Figure S1 corresponds to *Rumex hymenosepalus* aqueous solution absorption spectrum. A characteristic band centered at 278 nm is observed, associated with the electronic transitions of the aromatic rings conjugated with the carbonyl groups of polyphenolic compounds [82]. This absorption band in the nanoparticles UV–Vis spectra indicates that final products contain extract molecules that remain in them, Rivero-Cruz et. al. have reported four stilbenoids, two flavan-3-ols, and three anthraquinones isolated from *R. hymenosepalus* [83] and Rodríguez-León et. al. have performed a nuclear magnetic resonance study to determine that *Rumex hymenosepalus* contain important molecules as stilbene glycoside and epicatechin gallate and epigallocatechin gallate [61]. These molecules participate as reducing agents in nanoparticle synthesis. The process involves the deprotonation of some -OH groups of phenolic rings to form =CO groups. Polyphenolic molecules are oxidized, and the

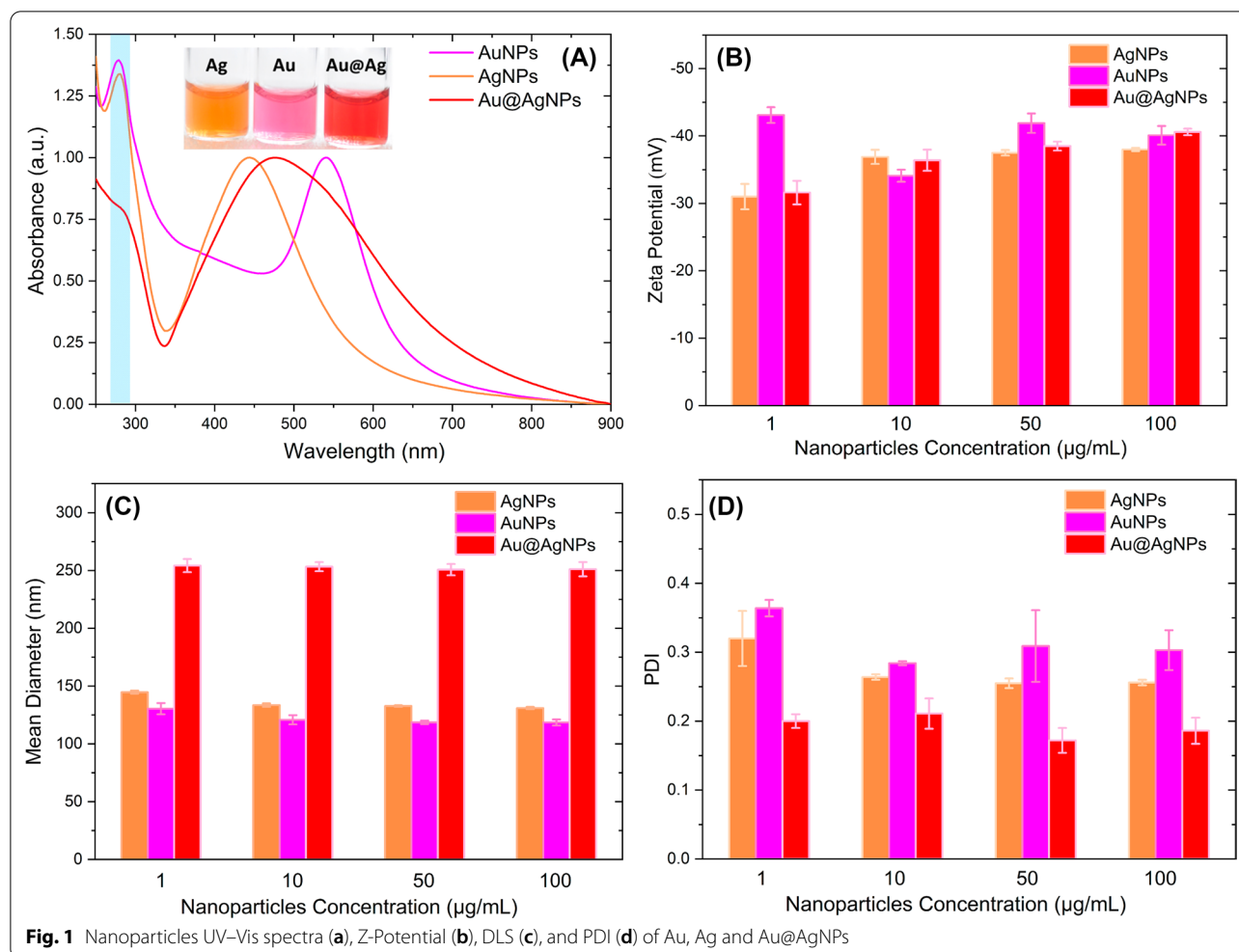


Fig. 1 Nanoparticles UV-Vis spectra (a), Z-Potential (b), DLS (c), and PDI (d) of Au, Ag and Au@AgNPs

released electrons are transferred to Ag^+ and Ag^{3+} ions to form Au^0 and Ag^0 .

Figure 1b shows the Zeta potentials values corresponding to AuNPs, AgNPs, and Au@AgNPs at concentrations of 1, 10, 50, and 100 $\mu\text{g/mL}$. Nanoparticles are dispersed in ultrapure water, and measurement was carried out by triplicate at 25 $^\circ\text{C}$. In general, throughout the concentration range, nanoparticles exhibit zeta potential values more negative than -30 mV, reaching values of -40 mV at a concentration of 100 $\mu\text{g/mL}$ for AuNPs and Au@AgNPs and -38 mV for AgNPs. These highly negative Zeta potential values indicate that nanoparticles experience repulsive interactions between them that prevent their aggregation and allow the long-term stability of metal colloids [84–86]. By correlating the UV-Vis spectroscopy results with the obtained Zeta potential values, we can establish that the highly negative values may be due to the complexing of

polyphenolic molecules of the extract onto the nanoparticle surface [87].

For biological applications, it is valuable to obtain nanoparticles population with monodisperse sizes [88], so Fig. 1c and d shows the DLS values corresponding to mean diameter and polydispersity index (PDI) for AuNPs, AgNPs, and Au@AgNPs at concentrations of 1, 10, 50, and 100 $\mu\text{g/mL}$. The mean diameter of Au@AgNPs is around 250 nm and kept constant as a function of concentration, in a similar manner for monometallic nanoparticles with a mean diameter around 122 and 135 nm for AuNPs and AgNPs, respectively. In the same case observe that values PDI is around 0.3 for monometallic nanoparticles and 0.2 for Au@AgNPs. These results, where the sizes do not vary with the concentration, indicate that the different nanoparticle systems have good stability presenting a moderate polydispersity of sizes ($0.3 \geq \text{PDI} \geq 0.2$).

The optical band gap of Tauc plot was computed (Additional file 1: Figure S2). Conduction band by

semiconductors materials have values $E_g < 3$ eV, as reference germanium have $E_g < 0.7$ eV and silicon is $E_g = 1.1$ eV [89]. In our case, the band gap for Au@AgNPs, AuNPs, and AgNPs is 1.93 eV, 2.03 eV, and 2.33 eV, respectively. This means that these materials are considered like semiconductors, and this feature was obtained for the quantum confinement effects that produce an increased energy gap, so nanomaterials can be used as sensors, batteries, and optoelectronic devices [64].

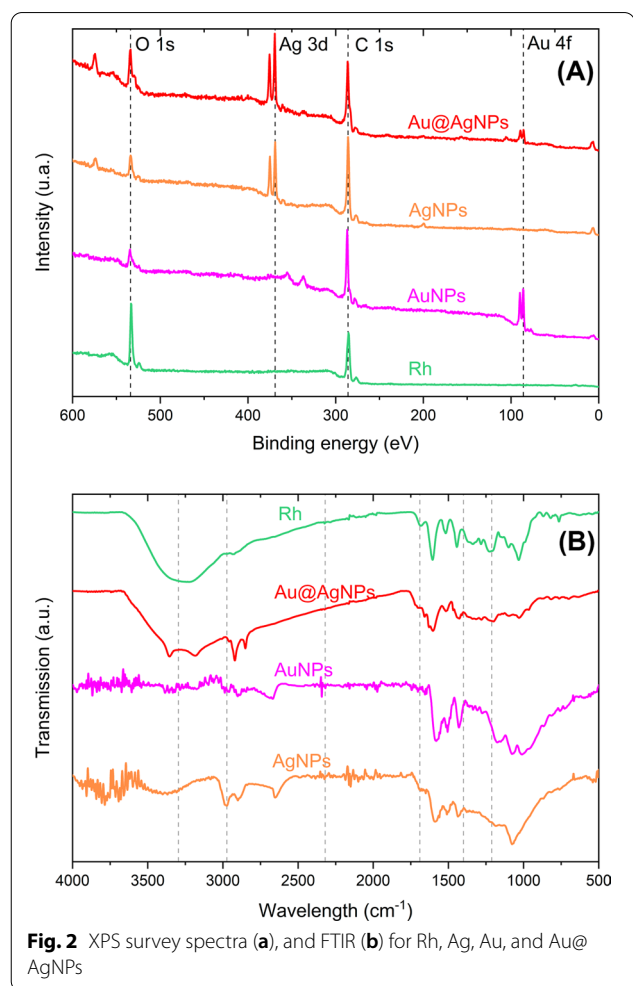
To establish if organic compounds are present in nanoparticles, these nanomaterials were characterized by XPS and FTIR. Figure 2a shows the survey spectra of the plant extract and nanoparticles. As can be seen, all nanoparticle systems present the characteristic signals associated with the elements carbon (C 1s, 284.6 eV) and oxygen (O 1s, 532.2 eV) from the *Rumex hymenosepalus* extract. This result confirms that organic molecules from extract are present in nanomaterials obtained. Additionally, high-resolution XPS spectra were obtained to analyze the oxidation states of silver and gold in the nanoparticles (Additional file 1: Figure S3). For AgNPs (Additional

file 1: Figure S3A), the signals at binding energies of 373.76 eV and 367.76 eV ($\Delta BE = 6.0$ eV) corresponding to the 3d_{3/2} and 3d_{5/2} spectral line can be associated with Ag⁰ (metallic silver). For AuNPs (Additional file 1: Figure S3B), the peak associated with 4f_{5/2} spin-orbital coupling is located on binding energy 87.65 eV. For 4f_{7/2}, spin-orbital coupling peak is located at 83.98 eV. The ratio of intensities ($I_{4f_{7/2}} > I_{4f_{5/2}}$), location, and separation between peaks ($\Delta BE = 3.67$ eV) confirm that gold ions (Au³⁺) are reduced completely to metallic gold Au⁰ [90]. For Au@AgNPs, high-resolution XPS spectra corresponding to silver and gold are showed in Additional file 1: Figure S3C and Figure S3-D, respectively. These spectra show the same behavior as their monometallic counterparts. This indicates that both silver and gold are zero-valent in the core@shell presentation.

FTIR in Fig. 2e shows at 3296 cm⁻¹ hydroxyl groups, 2974 cm⁻¹ (C–H) bind of the aromatic ring, 1689 cm⁻¹ associated with carbonyl group stretching (C=O), and 1689–1400 cm⁻¹ due to carboxylate bond (C–O) and stretching carbon–carbon bond and 1212 cm⁻¹ associated with phenol C–O stretching conjugated with AuNPs, 1049 cm⁻¹ C–O stretch mode of the catechin ester group molecules [88–90] and 799 cm⁻¹ the bending out of the plane in the phenol, C–H bending reported at 964.4, and 829.39 cm⁻¹ feature of resveratrol [91] shifted in Rh extract to 1031 and 867 cm⁻¹, respectively, and AuNPs, AgNPs, and Au@AgNPs are shifted too which is indicative of complexation of molecules polyphenolics of Rh extract with nanoparticles.

Figure 3a corresponds to a representative bright-field STEM micrograph of the Au@AgNPs system at low magnification (100 nm scale bar). A set of nanoparticles without agglomeration and with mostly quasi-spherical geometry can be seen. The same region is shown in dark field (HAADF) in Fig. 3b, and the core@shell structure can be observed, where can we distinguish Au-core looks more intense than Ag-shell, due to the difference in atomic number. Figure 3c and d corresponds to STEM higher magnification micrograph (scale bare 20 nm) of a nanoparticles group of system core@shell in a bright and dark field, respectively. Can be appreciated with clarity brilliant Au core and Ag shell lightly contrasted. These images show that the thickness of the Ag-shell varies between 3 and 5 nm. Additional file 1: Figure S4 corresponds to an individual images gallery where can be observed uniformity of Ag-shell.

Figure 4a, c, and e corresponds to micrograph TEM of representative nanoparticles systems AuNPs, AgNPs, and Au@AgNPs, respectively. In all cases, nanoparticles have sphere-like morphology and are shown well separated from each other. This can be explained by the extract molecules onto nanoparticle surfaces, acting as spacers



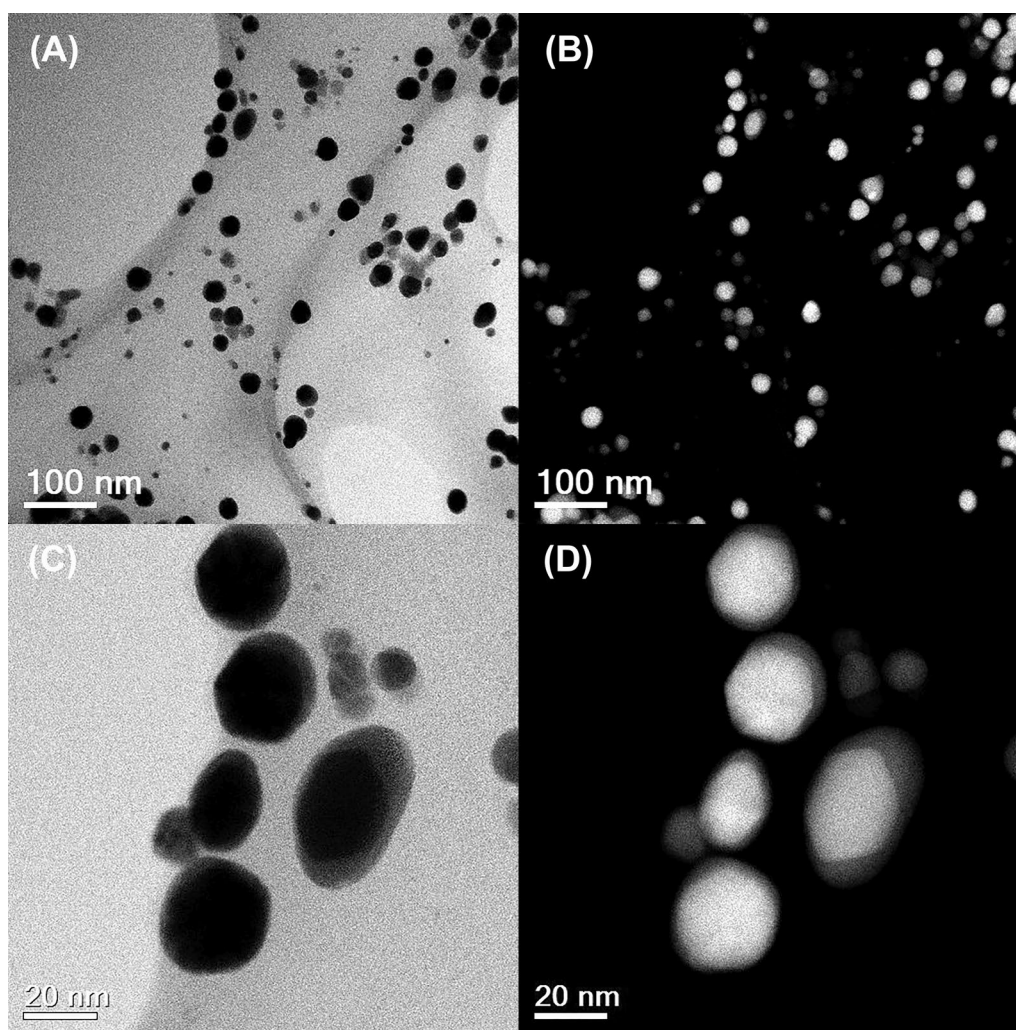


Fig. 3 Scanning Transmission Electron Microscopy at low magnification (scale bar 100 nm) of Au@AgNPs in Bright Field (a) and HAADF (b). A Small group of Au@AgNPs at higher magnification (scale bar 20 nm) in Bright Field (c) and HAADF (d)

between them. Figure 4b, d, and f shows histograms corresponding to size distribution obtained by TEM and performed with 500 nanoparticles collected from 15 to 20 micrographs for each nanomaterial. The histogram presents Gaussian distribution with a mean size of 24 ± 4 nm (AuNPs), 13 ± 3 nm (AgNPs), and 36 ± 11 nm (Au@AgNPs). The discrepancy in values between DLS and TEM measurements with size distribution graph is due to conditions micro-environmental around the nanoparticles, while DLS shows a diameter for a system that includes metal, hydrated coating, and solvent by comparison in TEM measurements is a dry system where measurement is over metal only, in particular, in DLS the molecules used for complexation of nanoparticles (reducing agents and stabilizers) are dispersants that

induce errors in sizing measurement and shifts its results to higher values [91].

Figure 5 corresponds to the Au@AgNPs HAADF-STEM micrographics. A single nanoparticle is shown in Fig. 5a with a gold nucleus and silver cover perfectly delimited, the atomic number (Z) changes through the interface Au@Ag, intensity variations can be quantified by HAADF-STEM [67].

The red square region is amplified to obtain an HRTEM micrograph of the shell portion (Fig. 5b), and then to verify the crystalline shell structure, the nanoparticle periphery region was analyzed (discontinued square) with the Digital Micrograph 3.0 software (Gatan). Fast Fourier Transform (FFT) image of the selected area was obtained (Fig. 5c). Using the Inverse Fast Fourier Transform was possible to estimate interplanar distances of

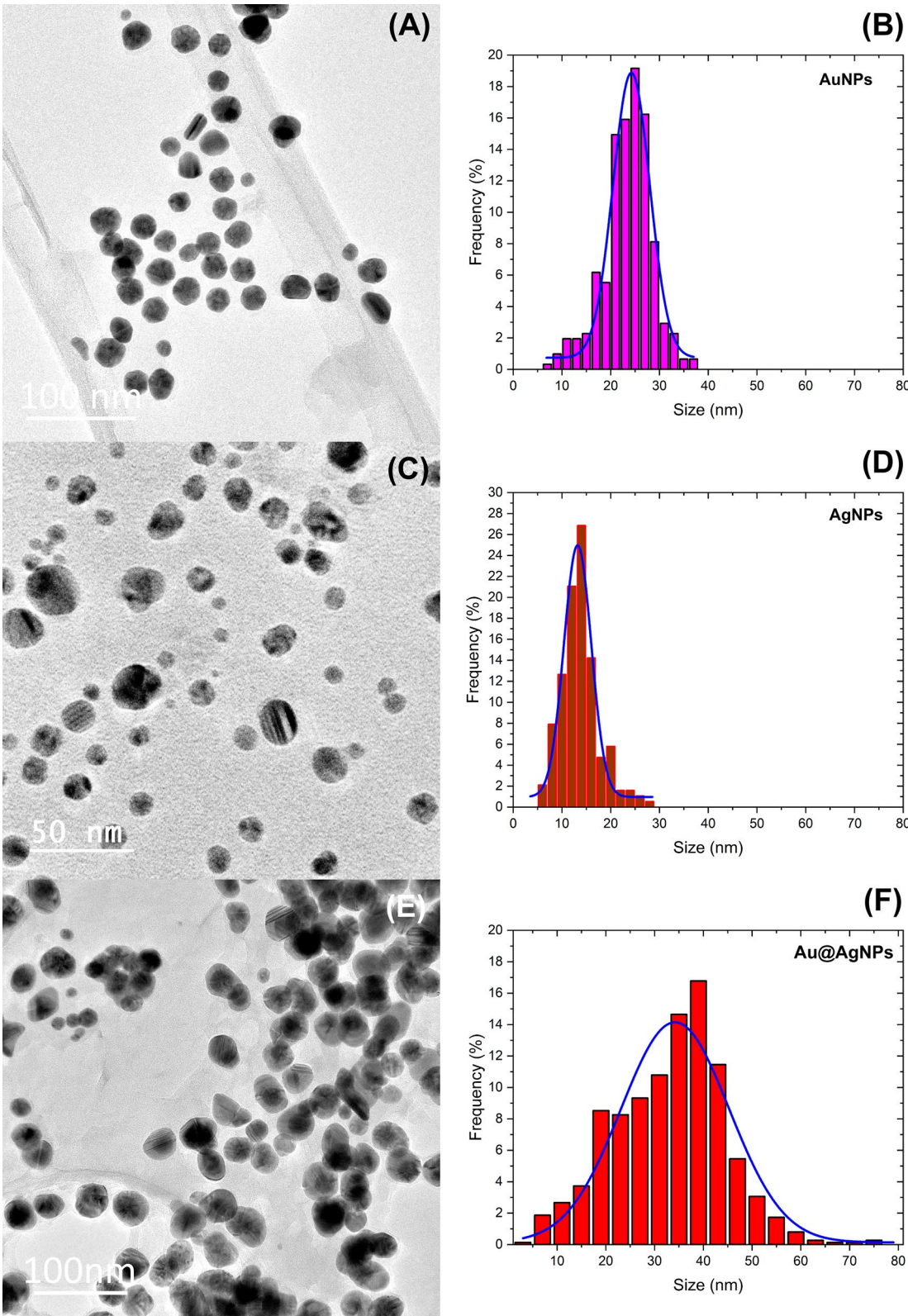


Fig. 4 TEM and size distribution of AuNPs in (a) and (b), AgNPs in (c) and (d), and Au@AgNPs in (e) and (f)

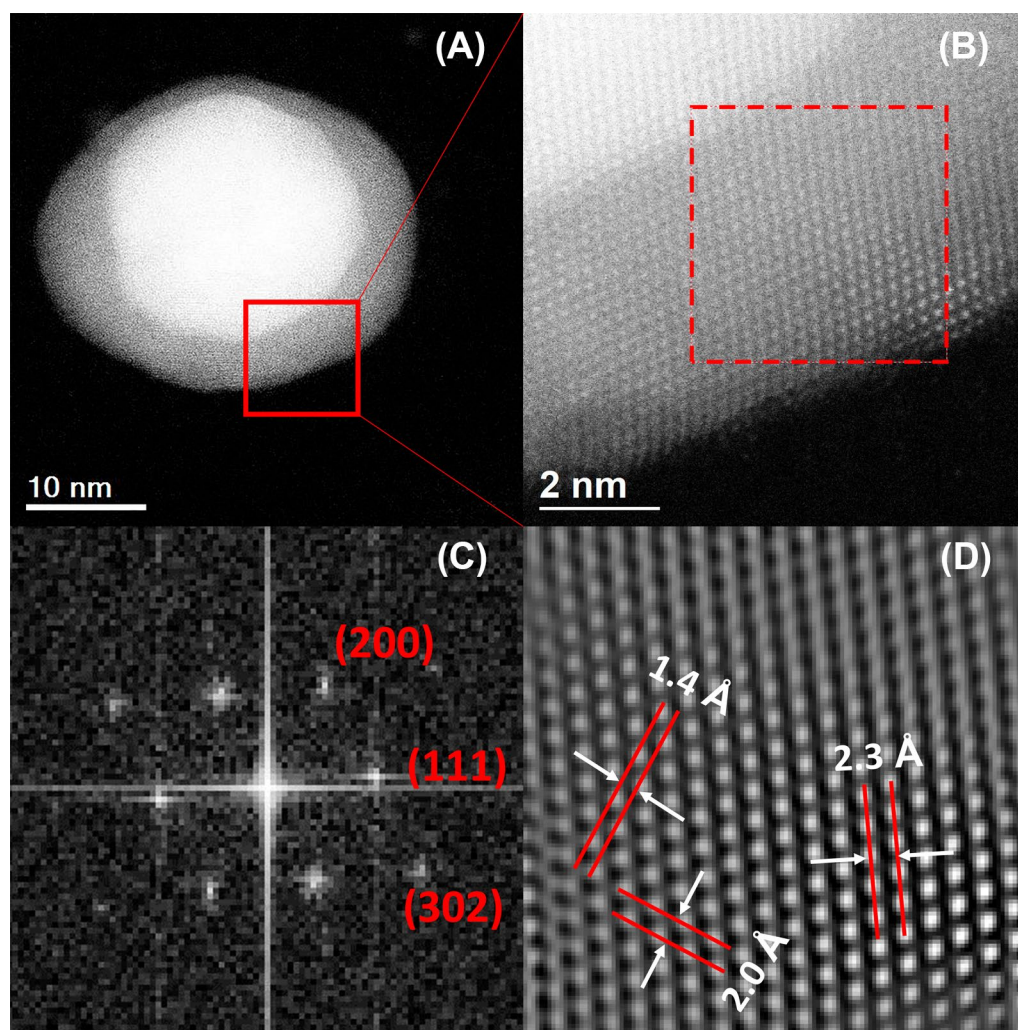


Fig. 5 Au@AgNPs HRTEM (a). Magnification from (a) of interface core-shell (b). FFT plot with Miller index (c) and integrated image from FFT (Inverse) with interplanar distance (d)

2.3 Å, 2.0 Å, and 1.4 Å in Fig. 5d. These distances can be assigned, respectively, to the crystalline planes (111), (200), and (220) of face-centered cubic (fcc) silver according to Inorganic Crystal Structure Database (ICSD) at the FIZ Karlsruhe–Leibniz Institute for Information Infrastructure, Germany or the electron crystallography software Jems (V 4-5430, JEMS-SAAS, Switzerland) [92]. A similar analysis of crystal structure by HRTEM was carried out for monometallic nanoparticles as illustrated in Additional file 1: Figures S5 (for AuNPs) and S6 (AgNPs). In both cases, crystal structure corresponds to face-centered cubic (fcc).

EDS chemical analysis shows the presence of both metals for a group of bimetallic Au@AgNPs observed by TEM (Fig. 6a) in proportions of the atomic weight percent 77% of Ag (shell) and 23% of Au (cores)

(Fig. 6b). In comparison, a single bimetallic (Fig. 6c) Au@AgNPs has proportions around 80% of Ag (shell) and 20% of Au (core) (Fig. 6d). To estimate the gold and silver atomic percentage on core@shell nanoparticles (Au@Ag), a quasi-spherical geometry approximation of nanoparticles morphology was considered. The AuNPs average diameter obtained from TEM size distribution ($\bar{D}_{Au} = 24$ nm) was used for core volume estimation (V_{Au}), and Au@AgNPs average diameter ($\bar{D}_{Au@Ag} = 36$ nm) for core@shell volume estimation ($V_{Au@Ag}$). So, shell volume is determined as $V_{Ag} = V_{Au@Ag} - V_{Au}$. Total atomic content of Au and Ag was calculated considering an fcc crystalline structure (4 atoms per unit cell) for both metals where the Au and Ag lattice parameters are 4.0783 Å and 4.0862 Å, respectively [93]. Atomic content estimation

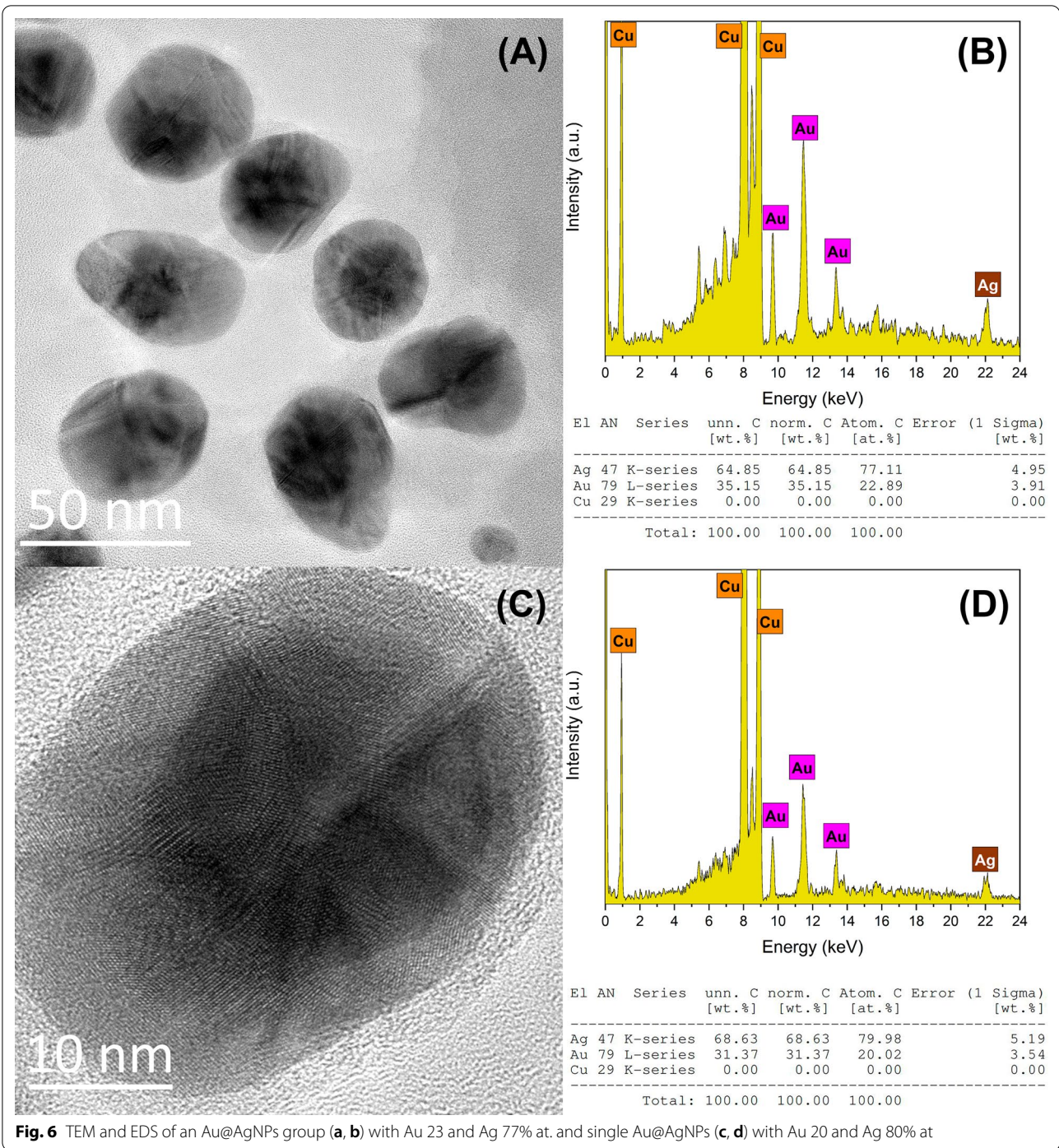


Fig. 6 TEM and EDS of an Au@AgNPs group (a, b) with Au 23 and Ag 77% at. and single Au@AgNPs (c, d) with Au 20 and Ag 80% at

by this procedure is 70% for Ag (Shell) and 30% Au (Core), which differs by 10% concerning the measurement obtained by EDS. Figure 7 shows a theoretical estimation of silver and gold content and how varies as the thickness of the shell increases and the size of the core is kept constant ($\bar{D}_{Au} = 24$ nm). It is observed that for Au@AgNPs with a diameter greater than 30.2 nm,

the atomic content of silver exceeds the content of gold. In Supplementary Material, a detailed description of calculation is carried out to obtain atomic contents percentage. Similar estimations of atomic percentages were carried out considering other Au-core diameters and varying Au@AgNPs diameter (Additional file 1: Figure S7A-B).

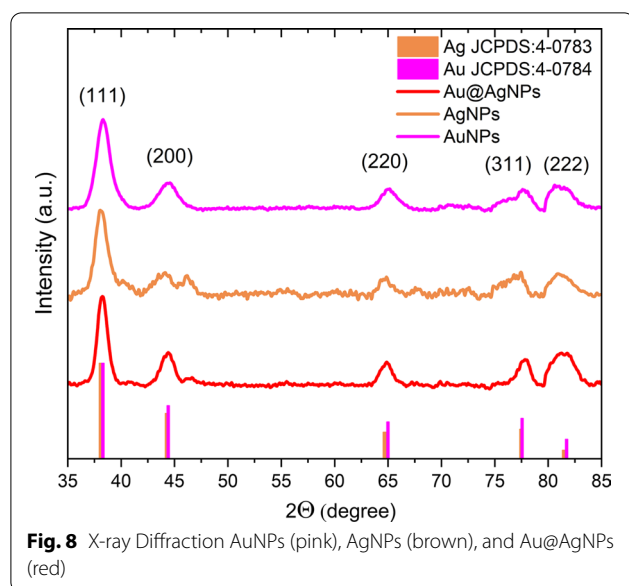
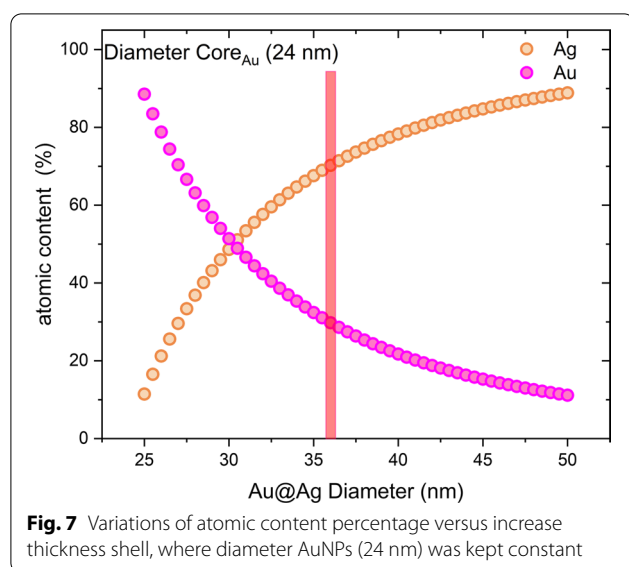


Figure 8 corresponds to XRD patterns for AuNPs and AgNPs as well as bimetallic Au@AgNPs. All the synthesized products have fcc crystalline structure as previously reported in the characterization by electron microscopy. Peaks for Au@AgNPs are located at 2θ diffraction angles of 38.25° , 44.4° , 64.9° , 77.85° , and 81.25° . As can be appreciated in the figure, the AgNPs and AuNPs diffraction peaks are found in the same positions mentioned with a difference of $\pm 0.5^\circ$. This is because Au and Ag have very similar lattice constants, so their diffraction patterns for fcc crystal structure are almost identical [94–96]. In this way, the diffraction peaks in Fig. 8 are assigned, respectively, to the crystalline planes (111), (200), (220), (311),

and (222) of the gold and silver fcc structure by JCPDS: 4-0783 and 4-0784 [97].

Antimicrobial Activity

Monometallic (AgNPs, AuNPs) and bimetallic (Au@AgNPs) materials were tested at four different concentrations: 1, 10, 50, and 100 $\mu\text{g/mL}$. Selected microorganisms to evaluate antimicrobial activity were yeast *Candida albicans*, Gram-positive bacteria *S. aureus*, and Gram-negative bacteria *E. coli*. Growth kinetics curves in a time-lapse of 24 h are shown in Fig. 9.

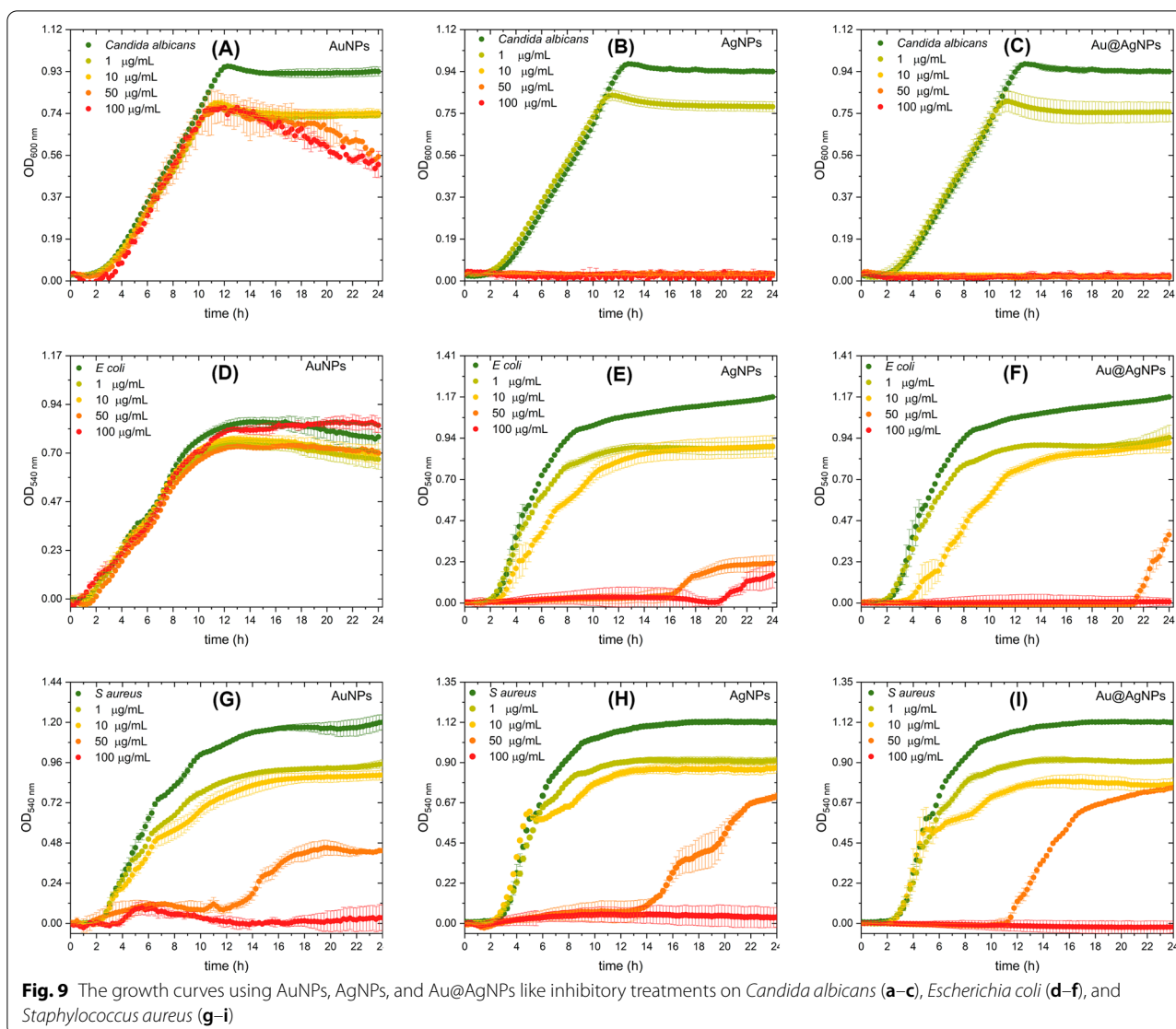
Candida albicans

AuNPs show no effect on growth kinetics until 10 h (Fig. 9a), varying in a dose-dependent manner the absorbance reached at 24 h. Interestingly, with 50 $\mu\text{g/mL}$ or more, the growth kinetic shows a steep negative slope from 10 h until reaching a 45% reduction at 24 h, which suggests an antifungal effect of these materials. This can be attributed to the ability of gold nanoparticles to interact with relevant proteins present in fungus such as H^+ -ATPase, affecting proton pump activity. This atrophying the ability of yeast to incorporate nutrients causing its death [61]. In Fig. 9b and c was observed that AgNPs and Au@AgNPs inhibit the growth of the yeast *Candida albicans* from 10 $\mu\text{g/mL}$. The determination of the MIC_{50} concentration for both materials was estimated from the dose–response curve shown in Additional file 1: Figure S8. MIC_{50} is defined as the concentration of nanoparticles that produces a 50% decrease in absorbance concerning the control (yeast without treatment). For AgNPs and Au@AgNPs, MIC_{50} were 2.21 $\mu\text{g/mL}$ and 2.37 $\mu\text{g/mL}$, respectively.

However, according to the EDS results (Fig. 9b), the silver content in Au@AgNPs is 64.85% mass. Thus, the concentration of silver in Au@AgNPs for MIC_{50} is 1.53 $\mu\text{g/mL}$, 30% lower than in the case of AgNPs. Padmos et al. have demonstrated that silver nanoparticles possess important antibacterial features, but are cytotoxic by mammalian cells this effect has reduced using bimetallic nanoparticles especially using gold in the core of bimetallic nanoparticles [35].

Escherichia coli

In Fig. 9d, AuNPs do not show significant inhibition ($< 15\%$) or affect the growth kinetics of *E. coli*. For AgNPs (Fig. 9e) at low concentrations, the Lag phase remains unchanged, but there is a marked decrease in growth ratio indicated by the slope decrement. At 50 $\mu\text{g/mL}$ Lag phase lasts up to 16 h and viability reaches a maximum of 20% at 24 h. For 100 $\mu\text{g/mL}$, an apparent detachment of



the growth phase of the microorganism is not observed. In Au@AgNPs (Fig. 9f), the first two concentrations do not show changes in their growth phase, but a phase delay of up to 2 h is observed compared to the control. It is interesting to note that the lag phase lasts up to 21 h for the 50 µg/mL concentration, finally there is no explicit growth behavior for the 100 µg/mL concentration.

Staphylococcus aureus

A comparative analysis of lag phase regrowth occurred after 12 h for Au (Fig. 9g), Ag (Fig. 9h), and Au@AgNPs (Fig. 9i) in the case of *S. aureus* at 50 µg/mL. For the highest concentration at 100 µg/mL, there is no growth of the bacteria. Additionally, we observe changes in the

slope of respect control for Au, Ag, and Au@AgNPs at 1 and 10 µg/mL.

AuNPs interaction with these Gram-positive bacteria could be due to the charged surface that causes an electrostatic interaction, destabilizing membrane structure. Similar results, but with higher NPs concentrations, are reported for AuNPs synthesized using *Ananas comosus* fruit extract as reducing agent [98] and blue-green alga *Spirulina platensis* protein [99]. Yang et al. show MIC > 500 µg/mL for *S. aureus* (CMCC(B)26003), our AuNPs has shown inhibition with 10 times less concentration; in this case, a critical synergy exists with polyphenols molecules on coating and stabilizing the surface of nanoparticle [100]. ROS is generated of less to higher intensity [101] by AuNPs, polyphenols (plant extracts),

and AgNPs, so AuNPs in synergy with resveratrol and epigallocatechin gallate (EGCG) promote antibacterial response over *S. aureus* [102] had the most feasible mechanism in this case. Penders et al. reported 250 and 500 $\mu\text{g/mL}$ of AuNPs-like antibacterial agents over *S. aureus* increases in bacterial growth lag time and antibacterial effect [61, 98, 99].

We believe that inhibition is caused by AgNPs [103] accumulation and diffusion on bacteria related to NPs surface charges that promote electrostatic interactions [104] with the bacteria's membrane leading to higher penetration and damage. We think this is a similar mechanism described for interactions between *E. coli* biofilms and AgNPs [105].

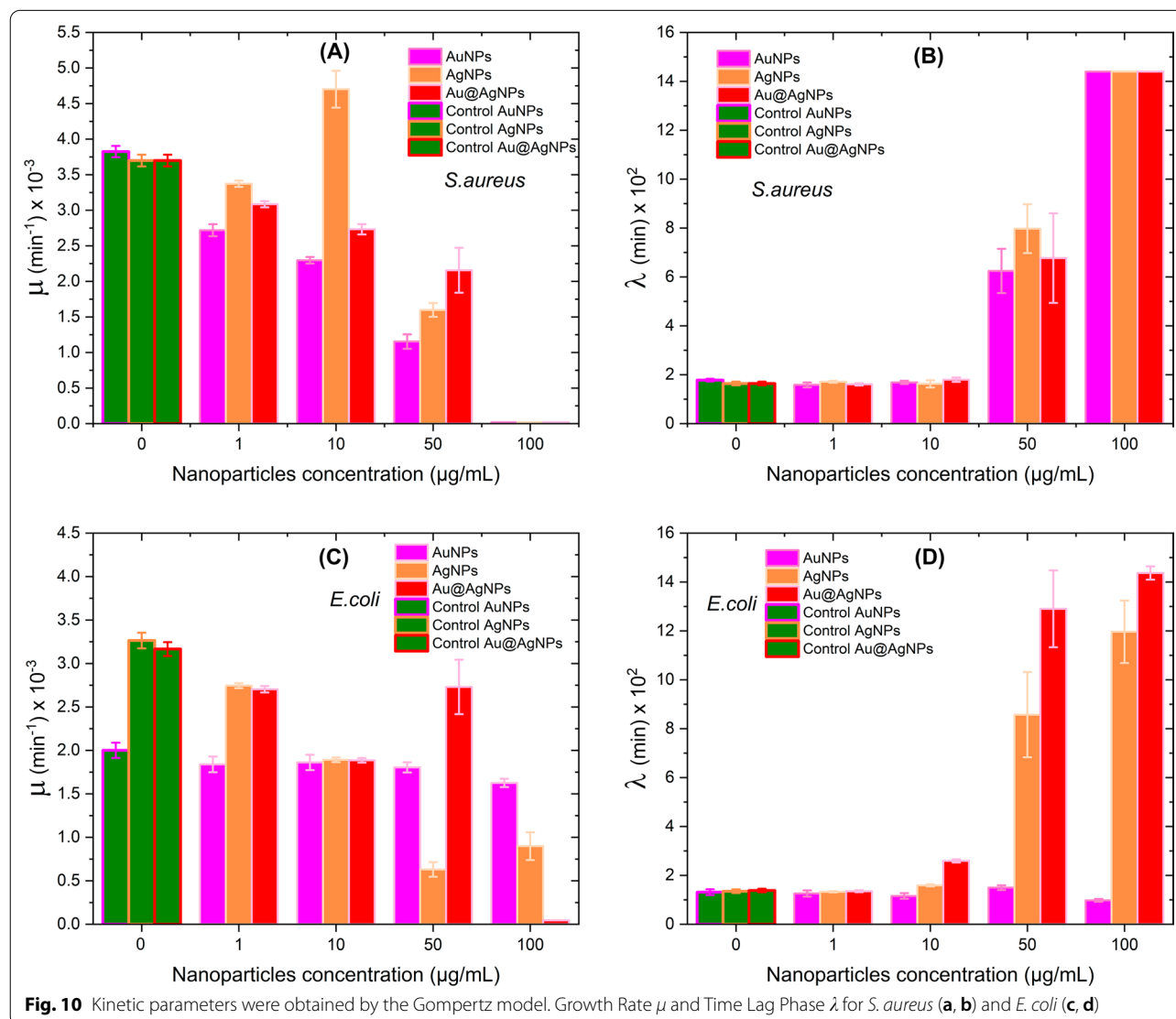
For Au@AgNPs, the obtained results are comparable to those reported by other workgroups [100, 101]; however, different authors suggest that the inhibition

of the growth of the microorganisms is directly related to the thickness of the shell [100, 101]. Core-shell NPs showed low cytotoxicity when tested in NIH-3T3 fibroblasts cells (normal mammalian cells) [35]. A lower proportion of silver in the shell of the Au@AgNPs shows similar results to AgNPs [100], and Au core potentializes antibacterial effect, and minimizes the cytotoxicity.

Curves Growth Analyzed by the Modified Gompertz Model

To know how the growth ratios (μ) and Lag phase (λ) are quantitatively modified, the growth curves of microorganisms exposed to different concentrations of nanomaterials (Fig. 10) were adjusted by the Gompertz model (Eq. 2).

In Fig. 10a, it can be seen that all nanomaterials produce a decrease in the replication rate of *S. aureus* populations when the concentration of nanoparticles



increases. This effect results in slightly higher sensitivity for AuNPs. At a concentration of 50 $\mu\text{g/mL}$, the growth ratio is only 30% concerning control (Additional file 1: Tables S1-S24); at a concentration of 100 $\mu\text{g/mL}$, all materials inhibit the growth of the *S. aureus* population. The behavior of the adaptive phase for *S. aureus* with the different treatments is shown in Fig. 10b. It is observed that there are no significant differences in the material used, and at 50 $\mu\text{g/mL}$, the Lag phase has increased by almost 5 times compared to the adaptive phase of *S. aureus* (Additional file 1: Tables S1-S24). In general, we can establish that the different nanomaterials evaluated in *S. aureus* reduce the replication rate and postpone the adaptive phase in a dose-dependent manner until its inhibition at 100 $\mu\text{g/mL}$.

Figure 10c clearly shows that AuNPs do not affect the growth ratio μ of *E. coli* bacteria. Meanwhile, AgNPs produce a decrease over μ , reaching a minimum value corresponding to 19% to the control (μ for *E. coli* without treatment) for 50 $\mu\text{g/mL}$ (see Additional file 1: Table S52). In contrast, Au@AgNPs completely inhibit the *E. coli* growth at 100 $\mu\text{g/mL}$. Analysis of the behavior of *E. coli* Lag phase exposed to different materials is shown in Fig. 10d. In this case, unlike Fig. 10b, each material has a characteristic response. Thus, AuNPs do not generate any modification in the adaptive phase of *E. coli*, while AgNPs and Au@AgNPs have a dose-dependent effect on the Lag phase, the latter material standing out. Thus, we can establish that AuNPs have no appreciable effect on *E. coli* bacteria, and Au@AgNPs can inhibit replication and, therefore, indefinitely postpone the Lag phase of *E. coli*. Interestingly, this effect is not achieved for AgNPs even though the net silver content is higher than in Au@AgNPs. This suggests that the core@shell presentation of both metals produces a synergy that favors antimicrobial activity. Feng et. al. have reported an electron compensation phenomena from Au to Ag in core-shell and alloy structures, which derive in enhance the cytotoxicity of nanoparticles but kept it the antibacterial properties, that means, a synergy between Au and Ag are assumed, due to observed differences between the monometallic and bimetallic materials [106], but more research is necessary.

Figure 11 shows the results of the direct count study of colonies of microorganisms exposed to nanomaterials. In general, the behavior of the microorganism populations reproduces the results obtained from the growth kinetics study (Fig. 7a, e, i). For example, in Fig. 11a, the population of microorganisms (represented logarithmically) decreases significantly only at 19 h where AuNPs have killed 92% of *C. albicans*. Interestingly, for nanoparticles containing silver (Fig. 11b, c) a more pronounced population decline is observed. Au@AgNPs system at 50 $\mu\text{g/mL}$, almost

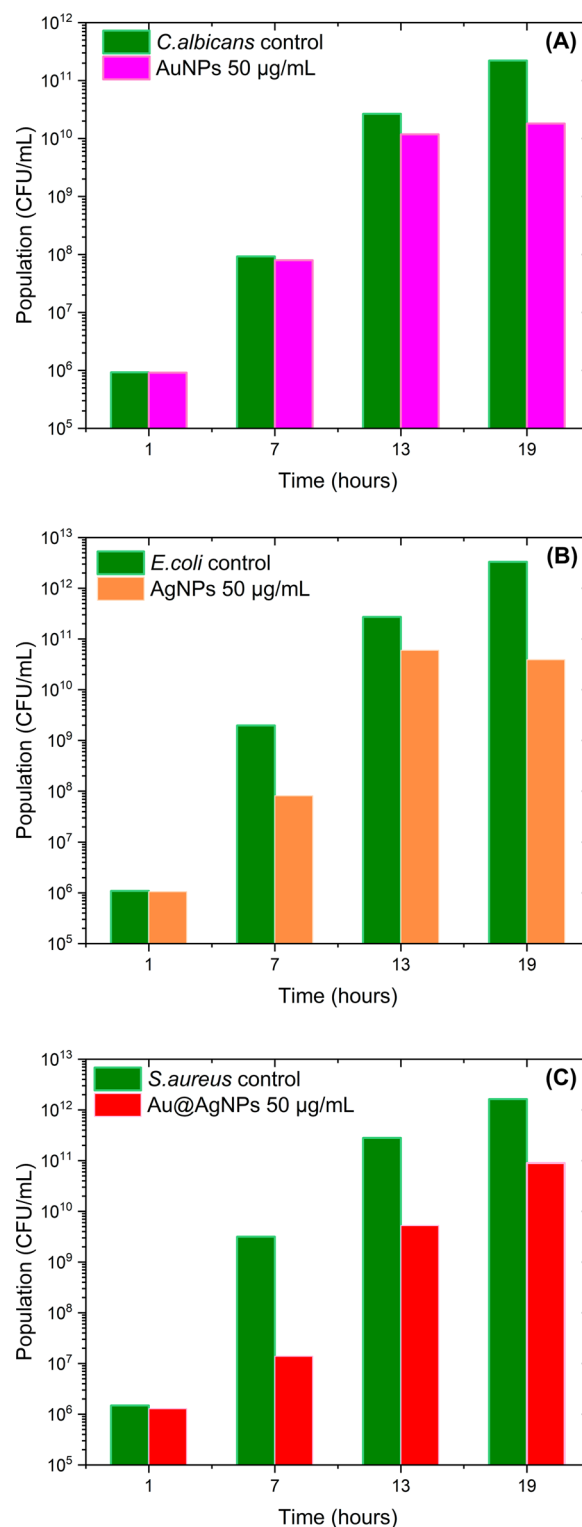


Fig. 11 Effect of nanoparticles over microorganisms growth *C. albicans* exposed to AuNPs (a), *E. coli* exposed to AgNPs (b), and *S. aureus* exposed to Au@AgNPs (c). All microorganisms were exposed at 50 $\mu\text{g/mL}$ nanoparticles concentration

entirely inhibits *S. aureus* at 7 h (99.5% of bacteria killed) although microorganism reactivates its growth for later times. MBC determination was not possible to obtain for tested concentrations (Additional file 1: Figure S9–11), according to experimental observation higher concentrations are required to show this effect. However, for *C. albicans*, AgNPs showed an MBC value of 50 µg/mL (Additional file 1: Table S55).

Conclusions

For the first time, the production of gold nanoparticles and core@shell (Au@Ag) is reported using a *Rumex hymenosepalus* root extract as a reducing agent. To obtain Au@AgNPs is proposed a two-step sequential method that produces particles with moderate polydispersity and homogeneous silver shell. Determination of the growth curves and their parameters obtained through the Gompertz model indicate different effects of the nanomaterials on evaluated microorganisms. Inhibitory effects of AuNPs over *S. aureus* are reached at a concentration of 5 times less to report for other AuNPs synthesized by different processes. This reveals the importance of the synthesis process followed and the environment on the surface of the nanoparticles. On the other hand, AgNPs and Au@AgNPs produce a great growth of the lag phase (> 12 h). However, bacteria can adapt and initiate their growth at these sub-inhibitory concentrations with the consequent risk of generating resistance to these nanomaterials. This highlights the importance of conducting growth kinetic studies that cover an appropriate period to discard a delayed growth. Interestingly, Gompertz's analysis indicates that Au@AgNPs present a higher effect on the growth kinetic of microorganisms than shown by monometallic nanoparticles, which can be attributed to a synergistic effect of both metals on the core@shell structure. Bactericidal effects are only achieved in *C. albicans* exposed to AgNPs. More experiments must be carried out on higher concentration ranges of these nanomaterials (> 200 µg/mL) to determine their MBC on the studied microorganisms.

Abbreviations

AuNPs: Gold nanoparticles; AgNPs: Silver nanoparticles; Au@AgNPs: Gold–silver bimetallic nanoparticles with core@shell structure; DLS: Dynamic light scattering; EDS: Energy-dispersive X-ray spectroscopy; EGCG: Epigallocatechin gallate; FTIR: Fourier transform infrared spectrometer; HAADF: High angle annular dark field images; MBC: Minimal bactericidal concentration; MIC: Minimum inhibitory concentration; Rh: *Rumex hymenosepalus* Root extract; TEM: Transmission electron microscopy; STEM: Scanning transmission electron microscope; UV-Vis: Spectroscopy ultraviolet–visible spectroscopy; XPS: X-ray photoelectron spectroscopy; XRD: X-ray diffraction.

Supplementary Information

The online version contains supplementary material available at <https://doi.org/10.1186/s11671-021-03572-5>.

Additional file 1. Figure S1 Corresponds to *Rumex hymenosepalus* aqueous solution absorption spectrum. Figure S2 A band gap Tauc plot of AgNPs, AuNPs, and Au@AgNPs. Figure S3 XPS high-resolution for AgNPs, AuNPs, and Au@AgNPs. Figure S4 STEM images gallery of individual Au@AgNPs. The first column corresponds to Bright Field images and the middle column to HAADF. The last column is shown manipulated images using ImageJ to enhance contrast. We can observe the uniformity of the Ag-shell. Figure S5 AuNPs HRTEM (A), region 1 FFT plot (B), and integrated image from FFT (C). Region 2 FFT plot is shown in (D) and integrated image from FFT with interplanar distances in (E). Figure S6 AgNPs HRTEM (A), FFT plot (B) and, integrated image from FFT with interplanar distances (C). Figure S7 Variations of atomic content percentage versus increase thickness shell. Figure S8 *C. albicans* dose-response curve comparative between Ag and Au@AgNPs. Table S1–S54. Adjust parameters of the curve by modified Gompertz Model (Origin 2018 software) and Physical Parameters of Bacterial Growth obtained with Adjust Parameters for *S. aureus*, *E. coli*, and *C. albicans* at concentrations 0, 1, 10, 50, and 100 µg/mL, respectively. Figure S9 Minimal Bactericidal Concentration determined for *E. coli* treated with nanoparticles and inoculated in Muller Hinton plate. AgNPs (A), AuNPs (B), and Au@AgNPs (C). Figure S10 Minimal Bactericidal Concentration determined for *S. aureus* treated with nanoparticles and inoculated in Muller Hinton plate. AgNPs (A), AuNPs (B), and Au@AgNPs (C). Figure S11. Minimal Bactericidal Concentration determined for *C. albicans* treated with nanoparticles and inoculated in Muller Hinton plate. AgNPs (A), AuNPs (B), and Au@AgNPs (C) Table S55. Minimal Bactericidal Concentration (MBC).

Acknowledgements

All authors wish to thank Dr. José Yacamán for the facilities provided in the characterization of the systems by electronic microscopy, as well as to the Kleberg Advanced Microscopy Center of the University of Texas at San Antonio Physics and Astronomy and the Laboratory of Biomaterials of Physics Department, University of Sonora. The authors are also grateful for the support of the SAGARPA Projects 17-PFA-IDTTT-001448-L000-DF, as well as the support provided by the Secretariat of Public Education (SEP) through PRODEP (Programa para el Desarrollo Profesional Docente) by the Postdoc fellowship 0511-6/17-4022 and AMH would like to thank Conacyt for Post-Doctoral Fellowship (2019-000019-01NACV-00449), Support Number 740180. All authors wish to thank the graduate program in nanotechnology at the University of Sonora for DLS, Zeta-sizer, characterizations support. JMAVN would like to thank Conacyt for Fellowship Number 748633. This publication was supported by the University of Sonora and the Professional Development Program (PRODEP) by SEP-México.

Authors' contributions

I.P. and R.L. contributed to the conception and experimental design. All authors contribute to the development of methodology and acquisition of data. V.N., I.P., R.L., R.B., and G.G. contributed to the writing and revision of the manuscript. All authors have read and approved the final manuscript.

Funding

Not applicable.

Availability of Data and Materials

All data generated or analyzed during this study are included in this article and its supplementary information file.

Declarations

Competing interests

The authors declare that they have no competing interests.

Author details

¹Nanotechnology Graduate Program, Department of Physics, University of Sonora, Rosales and Transversal, 83000 Hermosillo, Sonora, Mexico.

²Department of Chemical Engineering and Metallurgy, University

of Sonora, Rosales and Transversal, 83000 Hermosillo, Sonora, Mexico. ³Department of Research and Postgraduate in Food, University of Sonora, Rosales and Transversal, 83000 Hermosillo, Sonora, Mexico. ⁴Department of Physics, University of Sonora, Rosales and Transversal, 83000 Hermosillo, Sonora, Mexico. ⁵Food Science Coordination, Research Center in Food and Development (CIAD), Road Gustavo Enrique Astiazarán Rosas, No. 46, Col. La Victoria, 83304 Hermosillo, Sonora, Mexico. ⁶Department of Physic Researching, University of Sonora, Rosales and Transversal, 83000 Hermosillo, Sonora, Mexico. ⁷Health Sciences Graduate Program, Department of Biological Chemies, University of Sonora, Hermosillo, Sonora, Mexico. ⁸Department of Polymers and Materials Research, University of Sonora, Rosales and Transversal, 83000 Hermosillo, Sonora, Mexico.

Received: 11 January 2021 Accepted: 12 July 2021

Published online: 22 July 2021

References

- Munshi AM, Ho D, Saunders M et al (2016) Influence of aspect ratio of magnetite coated gold nanorods in hydrogen peroxide sensing. *Sens Actuators B Chem* 235:492–497
- Jiang Z, Le NDB, Gupta A, Rotello VM (2015) Cell surface-based sensing with metallic nanoparticles. *Chem Soc Rev* 44:4264–4274
- Gaines TW, Williams KR, Wagener KB (2016) ADMET. In: Al-mergen H, Xiao T (eds) *Petrochemical catalyst materials, processes, and emerging technologies*. IGI Global, Hershey, pp 1–21
- Liu X, Wang A, Yang X et al (2009) ChemInform abstract: Synthesis of thermally stable and highly active bimetallic Au-Ag nanoparticles on inert supports. *ChemInform*. <https://doi.org/10.1002/chin.200917217>
- Neppolian B, Wang C, Ashokkumar M (2014) Sonochemically synthesized mono and bimetallic Au–Ag reduced graphene oxide based nanocomposites with enhanced catalytic activity. *Ultrason Sonochem* 21:1948–1953
- Munshi AM, Agarwal V, Ho D et al (2016) Magnetically directed assembly of nanocrystals for catalytic control of a three-component coupling reaction. *Cryst Growth Des* 16:4773–4776
- Behera A, Mittu B, Padhi S et al (2020) Bimetallic nanoparticles: Green synthesis, applications, and future perspectives. In: Abd-El Salam K (ed) *Multifunctional hybrid nanomaterials for sustainable agri-food and ecosystems*. Elsevier, Hoboken, pp 639–682
- Majerič P, Jenko D, Friedrich B, Rudolf R (2018) Formation of bimetallic Fe/Au submicron particles with ultrasonic spray pyrolysis. *Metals (Basel)* 8:278
- Zhang L, Feng Q, Wang J et al (2015) Inside cover: microfluidic synthesis of rigid nanovesicles for hydrophilic reagents delivery (angew. Chem. Int. Ed. 13/2015). *Angew Chem Ed Int Engl* 54:3830–3830
- Liu D, Zhang H, Cito S et al (2017) Core/shell nanocomposites produced by superfast sequential microfluidic nanoprecipitation. *Nano Lett* 17:606–614
- Sebastián V, Zaborenko N, Gu L, Jensen KF (2017) Microfluidic assisted synthesis of hybrid Au–Pd dumbbell-like nanostructures: sequential addition of reagents and ultrasonic radiation. *Cryst Growth Des* 17:2700–2710
- Zaleska-Medynska A, Marchelek M, Diak M, Grabowska E (2016) Noble metal-based bimetallic nanoparticles: the effect of the structure on the optical, catalytic and photocatalytic properties. *Adv Colloid Interface Sci* 229:80–107
- Lee J-H, Shin Y, Lee W et al (2016) General and programmable synthesis of hybrid liposome/metal nanoparticles. *Sci Adv* 2:e1601838
- He Q, Liu J, Liu X et al (2019) A promising sensing platform toward dopamine using MnO₂ nanowires/electro-reduced graphene oxide composites. *Electrochim Acta* 296:683–692
- Wu Y, Deng P, Tian Y et al (2020) Rapid recognition and determination of tryptophan by carbon nanotubes and molecularly imprinted polymer-modified glassy carbon electrode. *Bioelectrochemistry* 131:107393
- Feng J, Deng P, Xiao J et al (2021) New voltammetric method for determination of tyrosine in foodstuffs using an oxygen-functionalized multi-walled carbon nanotubes modified acetylene black paste electrode. *J Food Compos Anal* 96:103708
- Tian B, Liu Q, Luo C et al (2020) Multifunctional ultrastretchable printed soft electronic devices for wearable applications. *Adv Electron Mater* 6:1900922
- Venditti I (2019) Engineered gold-based nanomaterials: morphologies and functionalities in biomedical applications. A mini review. *Bioengineering (Basel)* 6:53
- Ismail EH, Saqer AMA, Assirey E et al (2018) Successful green synthesis of gold nanoparticles using a *Corchorus olitorius* extract and their antiproliferative effect in cancer cells. *Int J Mol Sci*. <https://doi.org/10.3390/ijms19092612>
- Singh AK, Srivastava ON (2015) One-step green synthesis of gold nanoparticles using black cardamom and effect of pH on its synthesis. *Nanoscale Res Lett* 10:1055
- Rossi A, Donati S, Fontana L et al (2016) Negatively charged gold nanoparticles as a dexamethasone carrier: stability in biological media and bioactivity assessment in vitro. *RSC Adv* 6:99016–99022
- Venditti I, Iucci G, Fratoddi I et al (2020) Direct conjugation of Resveratrol on hydrophilic gold nanoparticles: structural and cytotoxic studies for biomedical applications. *Nanomaterials (Basel)*. <https://doi.org/10.3390/nano10101898>
- Aljabali A, Akkam Y, Al Zoubi M et al (2018) Synthesis of gold nanoparticles using leaf extract of *Ziziphus zizyphus* and their antimicrobial activity. *Nanomaterials (Basel)* 8:174
- Shu M, He F, Li Z et al (2020) Biosynthesis and antibacterial activity of silver nanoparticles using yeast extract as reducing and capping agents. *Nanoscale Res Lett* 15:14
- Mochi F, Burratti L, Fratoddi I et al (2018) Plasmonic sensor based on interaction between silver nanoparticles and Ni₂₊ or Co₂₊ in water. *Nanomaterials (Basel)*. <https://doi.org/10.3390/nano8070488>
- Chung I-M, Park I, Seung-Hyun K et al (2016) Plant-mediated synthesis of silver nanoparticles: their characteristic properties and therapeutic applications. *Nanoscale Res Lett* 11:40
- Amina M, Al Musayeb NM, Alarfaj NA et al (2020) Antibacterial and immunomodulatory potentials of biosynthesized Ag, Au, Ag-Au bimetallic alloy nanoparticles using the *Asparagus racemosus* root extract. *Nanomaterials (Basel)* 10:2453
- Banerjee M, Sharma S, Chattopadhyay A, Ghosh SS (2011) Enhanced antibacterial activity of bimetallic gold–silver core–shell nanoparticles at low silver concentration. *Nanoscale* 3:5120–5125
- Lu Z, Zhang J, Yu Z et al (2017) Vancomycin-hybrid bimetallic Au/Ag composite nanoparticles: preparation of the nanoparticles and characterization of the antibacterial activity. *New J Chem* 41:5276–5279
- Franci G, Falanga A, Galdiero S et al (2015) Silver nanoparticles as potential antibacterial agents. *Molecules* 20:8856–8874
- Thanh NTK, Green LAW (2010) Functionalisation of nanoparticles for biomedical applications. *Nano Today* 5:213–230
- Karam TE, Smith HT, Haber LH (2015) Enhanced photothermal effects and excited-state dynamics of plasmonic size-controlled gold–silver–gold core–shell–shell nanoparticles. *J Phys Chem C Nanomater Interfaces* 119:18573–18580
- Ding X, Yuan P, Gao N et al (2017) Au-Ag core–shell nanoparticles for simultaneous bacterial imaging and synergistic antibacterial activity. *Nanomedicine* 13:297–305
- Paszkievicz M, Gołębiewska A, Rajski Ł et al (2016) Synthesis and characterization of monometallic (Ag, Cu) and bimetallic Ag-Cu particles for antibacterial and antifungal applications. *J Nanomater* 2016:1–11
- Padmos JD, Langman M, MacDonald K et al (2015) Correlating the atomic structure of bimetallic silver–gold nanoparticles to their antibacterial and cytotoxic activities. *J Phys Chem C Nanomater Interfaces* 119:7472–7482
- Peng X, Pan Q, Rempel GL (2008) Bimetallic dendrimer-encapsulated nanoparticles as catalysts: a review of the research advances. *Chem Soc Rev* 37:1619–1628
- Toshima N, Yonezawa T (1998) Bimetallic nanoparticles—novel materials for chemical and physical applications. *New J Chem* 22:1179–1201
- Scott RWJ, Wilson OM, Oh S-K (2004) Bimetallic palladium–gold dendrimer-encapsulated catalysts. *J Am Chem Soc* 126(47):15583–15591
- Mondal S, Roy N, Laskar RA et al (2011) Biogenic synthesis of Ag, Au and bimetallic Au/Ag alloy nanoparticles using aqueous extract of

- mahogany (Swietenia mahogani JACQ.) leaves. *Colloids Surf B Biointerfaces* 82:497–504
40. Tamlin situ biosynthesis of Ag, Au and bimetallic nanoparticles using Piper pedicellatum C. *Green Chemistry Approach*, DC
 41. Roopan SM, Surendra TV, Elango G, Kumar SHS (2014) Biosynthetic trends and future aspects of bimetallic nanoparticles and its medicinal applications. *Appl Microbiol Biotechnol* 98:5289–5300
 42. Huo D, He J, Li H et al (2014) Fabrication of Au@Ag core-shell NPs as enhanced CT contrast agents with broad antibacterial properties. *Colloids Surf B Biointerfaces* 117:29–35
 43. Balati A, Shahbazi A, Amini MM, Hashemi SH (2015) Adsorption of polycyclic aromatic hydrocarbons from wastewater by using silica-based organic-inorganic nanohybrid material. *J Water Reuse Desalination* 5:50–63
 44. Balati A, Shahbazi A, Amini MM et al (2014) Comparison of the efficiency of mesoporous silicas as adsorbents for removing naphthalene from contaminated water. *Eur J Environ Sci* 4:69–76
 45. Balati A, Ghanbari M, Sara BK, Amini MM (2017) Functionalization of graphene oxide with 9-aminoanthracene for the adsorptive removal of persistent aromatic pollutants from aqueous solution. *Acta Chim Slov* 64:479–490
 46. Rónavári A, Igaz N, Adamecz DI et al (2021) Green silver and gold nanoparticles: Biological synthesis approaches and potentials for biomedical applications. *Molecules* 26:844
 47. Singh P, Pandit S, Garnæs J et al (2018) Green synthesis of gold and silver nanoparticles from *Cannabis sativa* (industrial hemp) and their capacity for biofilm inhibition. *Int J Nanomed* 13:3571–3591
 48. Lee KX, Shameli K, Yew YP et al (2020) Recent developments in the facile bio-synthesis of gold nanoparticles (AuNPs) and their biomedical applications. *Int J Nanomed* 15:275–300
 49. Castillo-Henríquez L, Alfaro-Aguilar K, Ugalde-Álvarez J et al (2020) Green synthesis of gold and silver nanoparticles from plant extracts and their possible applications as antimicrobial agents in the agricultural area. *Nanomaterials (Basel)* 10:1763
 50. Islam NU, Amin R, Shahid M et al (2017) A multi-target therapeutic potential of *Prunus domestica* gum stabilized nanoparticles exhibited prospective anticancer, antibacterial, urease-inhibition, anti-inflammatory and analgesic properties. *BMC Complement Altern Med* 17:276
 51. Mukherjee S, Chowdhury D, Kotcherlakota R et al (2014) Potential theranostics application of bio-synthesized silver nanoparticles (4-in-1 system). *Theranostics* 4:316–335
 52. Ahmad S, Munir S, Zeb N et al (2019) Green nanotechnology: a review on green synthesis of silver nanoparticles—an ecofriendly approach. *Int J Nanomed* 14:5087–5107
 53. Nayem SMA, Sultana N, Haque MA et al (2020) Green synthesis of gold and silver nanoparticles by using *Amorphophallus paeoniifolius* tuber extract and evaluation of their antibacterial activity. *Molecules*. <https://doi.org/10.3390/molecules25204773>
 54. Khodadadi S, Mahdinezhad N, Fazeli-Nasab B et al (2021) Investigating the possibility of green synthesis of silver nanoparticles using *Vaccinium arctostaphylos* extract and evaluating its antibacterial properties. *Biomed Res Int* 2021:5572252
 55. Ramos RMCR, Regulacio MD (2021) Controllable synthesis of bimetallic nanostructures using biogenic reagents: a green perspective. *ACS Omega* 6:7212–7228
 56. Shin Y, Bae I-T, Arey BW, Exarhos GJ (2008) Facile stabilization of gold-silver alloy nanoparticles on cellulose nanocrystal. *J Phys Chem C Nanomater Interfaces* 112:4844–4848
 57. An Q, Yu M, Zhang Y et al (2012) Fe₃O₄@carbon microsphere supported Ag-Au bimetallic nanocrystals with the enhanced catalytic activity and selectivity for the reduction of nitroaromatic compounds. *J Phys Chem C Nanomater Interfaces* 116:22432–22440
 58. Jagannathan A, Gangareddy J, Rajaramakrishna R et al (2021) Precursor based tuning of the nonlinear optical properties of Au-Ag bimetallic nanoparticles doped in oxy-fluoroborate glasses. *J Non Cryst Solids* 561:120766
 59. Balati A, Tek S, Nash K, Shipley H (2019) Nanoarchitecture of TiO₂ microspheres with expanded lattice interlayers and its heterojunction to the laser modified black TiO₂ using pulsed laser ablation in liquid with improved photocatalytic performance under visible light irradiation. *J Colloid Interface Sci* 541:234–248
 60. Cheng Z-Q, Li Z-W, Yao R et al (2020) Improved SERS performance and catalytic activity of dendritic Au/Ag bimetallic nanostructures based on Ag dendrites. *Nanoscale Res Lett* 15:117
 61. Rodríguez-León E, Iñiguez-Palomares R, Navarro RE et al (2013) Synthesis of silver nanoparticles using reducing agents obtained from natural sources (*Rumex hymenosepalus* extracts). *Nanoscale Res Lett* 8:318
 62. Hughes JM, Budd PM, Grieve A et al (2015) Highly monodisperse, lanthanide-containing polystyrene nanoparticles as potential standard reference materials for environmental “nano” fate analysis. *J Appl Polym Sci*. <https://doi.org/10.1002/app.42061>
 63. Sneha M, Sundaram NM, Kandaswamy A (2016) Synthesis and characterization of magnetite/hydroxyapatite tubes using natural template for biomedical applications. *Bull Mater Sci (India)* 39:509–517
 64. Mistry H, Thakor R, Patil C et al (2021) Biogenically proficient synthesis and characterization of silver nanoparticles employing marine procured fungi *Aspergillus brunneoviolaceus* along with their antibacterial and antioxidative potency. *Biotechnol Lett* 43:307–316
 65. Mishra M (2018) Composite of discotic liquid crystal and gold nanoparticles: a cooperative band gap study. *Phase Transitions* 91:752–758
 66. Rodríguez-León E, Rodríguez-Vázquez BE, Martínez-Higuera A et al (2019) Synthesis of gold nanoparticles using *Mimosa tenuiflora* extract, assessments of cytotoxicity, cellular uptake, and catalysis. *Nanoscale Res Lett* 14:334
 67. Fernández-Delgado N, Herrera M, Pizarro J et al (2018) HAADF-STEM for the analysis of core-shell quantum dots. *J Mater Sci* 53:15226–15236
 68. Vanrompay H, Skorikov A, Bladt E et al (2021) Fast versus conventional HAADF-STEM tomography of nanoparticles: advantages and challenges. *Ultramicroscopy* 221:113191
 69. Li B, Qiu Y, Shi H, Yin H (2016) The importance of lag time extension in determining bacterial resistance to antibiotics. *Analyst* 141:3059–3067
 70. Zwietering MH, Jongenburger I, Rombouts FM, van ’t Riet K, (1990) Modeling of the bacterial growth curve. *Appl Environ Microbiol* 56:1875–1881
 71. Chatterjee T, Chatterjee BK, Majumdar D, Chakrabarti P (2015) Antibacterial effect of silver nanoparticles and the modeling of bacterial growth kinetics using a modified Gompertz model. *Biochim Biophys Acta* 1850:299–306
 72. Penders J, Stolzoff M, Hickey DJ et al (2017) Shape-dependent antibacterial effects of non-cytotoxic gold nanoparticles. *Int J Nanomed* 12:2457–2468
 73. Lambert RJ, Pearson J (2000) Susceptibility testing: accurate and reproducible minimum inhibitory concentration (MIC) and non-inhibitory concentration (NIC) values. *J Appl Microbiol* 88:784–790
 74. Dartevelle P, Ehlinger C, Zaet A et al (2018) D-Cateslytin: a new antifungal agent for the treatment of oral *Candida albicans* associated infections. *Sci Rep*. <https://doi.org/10.1038/s41598-018-27417-x>
 75. Lomeli-Marroquín D, Medina Cruz D, Nieto-Argüello A et al (2019) Starch-mediated synthesis of mono- and bimetallic silver/gold nanoparticles as antimicrobial and anticancer agents. *Int J Nanomed* 14:2171–2190
 76. Chankaew C, Somsri S, Tapala W et al (2018) Kaffir lime leaf extract mediated synthesis, anticancer activities and antibacterial kinetics of Ag and Ag/AgCl nanoparticles. *Particuology* 40:160–168
 77. Hernández-Díaz JA, Garza-García JJO, Zamudio-Ojeda A et al (2020) Plant-mediated synthesis of nanoparticles and their antimicrobial activity against phytopathogens. *J Sci Food Agric*. <https://doi.org/10.1002/jsfa.10767>
 78. Tjørve KMC, Tjørve E (2017) The use of Gompertz models in growth analyses, and new Gompertz-model approach: an addition to the unified-Richards family. *PLoS ONE* 12:e0178691
 79. Sinha T, Ahmaruzzaman M (2015) A novel and greener approach for shape controlled synthesis of gold and gold-silver core shell nanostructure and their application in optical coatings. *Spectrochim Acta A Mol Biomol Spectrosc* 145:280–288
 80. Bu Y, Lee S-W (2015) The characteristic Ag(core)Au(shell) nanoparticles as SERS substrates in detecting dopamine molecules at various pH ranges. *Int J Nanomed* 10(Spec Iss):47–54
 81. Samal AK, Polavarapu L, Rodal-Cedeira S et al (2013) Size tunable Au@Ag core-shell nanoparticles: synthesis and surface-enhanced Raman scattering properties. *Langmuir* 29:15076–15082

82. Lopes LCS, Brito LM, Bezerra TT et al (2018) Silver and gold nanoparticles from tannic acid: synthesis, characterization and evaluation of antileishmanial and cytotoxic activities. *An Acad Bras Cienc* 90:2679–2689
83. Rivero-Cruz I, Acevedo L, Guerrero JA et al (2005) Antimycobacterial agents from selected Mexican medicinal plants. *J Pharm Pharmacol* 57:1117–1126
84. Saratale RG, Shin HS, Kumar G et al (2018) Exploiting antidiabetic activity of silver nanoparticles synthesized using *Punica granatum* leaves and anticancer potential against human liver cancer cells (HepG2). *Artif Cells Nanomed Biotechnol* 46:211–222
85. Rezazadeh NH, Buazar F, Matroodi S (2020) Synergistic effects of combinatorial chitosan and polyphenol biomolecules on enhanced antibacterial activity of biofunctionalized silver nanoparticles. *Sci Rep* 10:19615
86. Ajitha B, Ashok Kumar Reddy Y, Sreedhara Reddy P (2015) Green synthesis and characterization of silver nanoparticles using *Lantana camara* leaf extract. *Mater Sci Eng C Mater Biol Appl* 49:373–381
87. Maddinedi SB, Mandal BK, Maddili SK (2017) Biofabrication of size controllable silver nanoparticles—a green approach. *J Photochem Photobiol B* 167:236–241
88. Johnston ST, Faria M, Crampin EJ (2018) An analytical approach for quantifying the influence of nanoparticle polydispersity on cellular delivered dose. *J R Soc Interface*. <https://doi.org/10.1098/rsif.2018.0364>
89. Zhang JJ, Ni J (2016) Germanium. In: Hashmi S (ed) Reference module in materials science and materials engineering. Elsevier, Amsterdam
90. Ghodake G, Shinde S, Kadam A et al (2020) Gallic acid-functionalized silver nanoparticles as colorimetric and spectrophotometric probe for detection of Al_3^+ in aqueous medium. *J Ind Eng Chem* 82:243–253
91. Souza TGF, Ciminelli VST, Mohallem NDS (2016) A comparison of TEM and DLS methods to characterize size distribution of ceramic nanoparticles. *J Phys Conf Ser* 733:e12039
92. Steinhoff B, Müller J, Mozhayeva D et al (2020) Investigation of the fate of silver and titanium dioxide nanoparticles in model wastewater effluents via selected area electron diffraction. *Environ Sci Technol* 54:8681–8689
93. Šrnová-Šloufová I, Lednický F, Gemperle A, Gemperlová J (2000) Core–shell (Ag)Au bimetallic nanoparticles: analysis of transmission electron microscopy images. *Langmuir* 16:9928–9935
94. Alarfaj NA, Altamimi SA, El-Tohamy MF, Almahri AM (2019) Exploitation of localized surface plasmon resonance of silver/gold nanoparticles for the fluorescence quantification of angiotensin II receptor antagonists in their tablets and bio-samples. *New J Chem* 43:492–503
95. Doan V-D, Huynh B-A, Nguyen T-D et al (2020) Biosynthesis of silver and gold nanoparticles using aqueous extract of *Codonopsis pilosula* roots for antibacterial and catalytic applications. *J Nanomater* 2020:1–18
96. Meena Kumari M, Jacob J, Philip D (2015) Green synthesis and applications of Au-Ag bimetallic nanoparticles. *Spectrochim Acta A Mol Biomol Spectrosc* 137:185–192
97. Yallappa S, Manjanna J, Dhananjaya BL (2015) Phytosynthesis of stable Au, Ag and Au-Ag alloy nanoparticles using *J. sambac* leaves extract, and their enhanced antimicrobial activity in presence of organic antimicrobials. *Spectrochim Acta A Mol Biomol Spectrosc* 137:236–243
98. Bindhu MR, Umadevi M (2014) Antibacterial activities of green synthesized gold nanoparticles. *Mater Lett* 120:122–125
99. Suganya KSU, Govindaraju K, Kumar VG et al (2015) Blue green alga mediated synthesis of gold nanoparticles and its antibacterial efficacy against Gram positive organisms. *Mater Sci Eng C Mater Biol Appl* 47:351–356
100. Yang L, Yan W, Wang H et al (2017) Shell thickness-dependent antibacterial activity and biocompatibility of gold@silver core–shell nanoparticles. *RSC Adv* 7:11355–11361
101. Tsai T-T, Huang T-H, Chang C-J et al (2017) Antibacterial cellulose paper made with silver-coated gold nanoparticles. *Sci Rep* 7:3155
102. Bouarab-Chibane L, Forquet V, Lantéri P et al (2019) Antibacterial properties of polyphenols: characterization and QSAR (Quantitative Structure-Activity Relationship) models. *Front Microbiol* 10:829
103. Koduru JR, Kailasa SK, Bhamore JR et al (2018) Phytochemical-assisted synthetic approaches for silver nanoparticles antimicrobial applications: a review. *Adv Colloid Interface Sci* 256:326–339
104. Golmohamadi M, Clark RJ, Veinot JGC, Wilkinson KJ (2013) The role of charge on the diffusion of solutes and nanoparticles (silicon nanocrystals, $nTiO_2$, nAu) in a biofilm. *Environ Chem* 10:34
105. Choi O, Yu C-P, Esteban Fernández G, Hu Z (2010) Interactions of nanosilver with *Escherichia coli* cells in planktonic and biofilm cultures. *Water Res* 44:6095–6103
106. Feng Y, Wang G, Chang Y et al (2019) Electron compensation effect suppressed silver ion release and contributed safety of Au@Ag core–shell nanoparticles. *Nano Lett* 19:4478–4489

Publisher's Note

Springer Nature remains neutral with regard to jurisdictional claims in published maps and institutional affiliations.

Submit your manuscript to a SpringerOpen[®] journal and benefit from:

- Convenient online submission
- Rigorous peer review
- Open access: articles freely available online
- High visibility within the field
- Retaining the copyright to your article

Submit your next manuscript at ► [springeropen.com](https://www.springeropen.com)